EXAMINATION OF ICING MECHANISM ON AIRCRAFT WINGS WITH NUMERICAL METHODS

CEM ONAY

SEPTEMBER 2025

ÇANKAYA UNIVERSITY

GRADUATE SCHOOL

MECHANICAL ENGINEERING DEPARTMENT
MECHANICAL ENGINEERING MASTER'S THESIS

EXAMINATION OF ICING MECHANISM ON AIRCRAFT WINGS WITH NUMERICAL METHODS

CEM ONAY

SEPTEMBER 2025

ABSTRACT

EXAMINATION OF ICING MECHANISM ON AIRCRAFT WINGS WITH NUMERICAL METHODS

ONAY, CEM

MECHANICAL ENGINEERING MASTER'S THESIS

Supervisor: Assoc. Prof. Dr. Ülkü Ece AYLI

Co-Supervisor: Assist. Prof. Dr. Eyup KOÇAK

September 2025, 82 Pages

In this thesis study, the effects of key parameters such as angle of attack (AoA), liquid water content (LWC), median volumetric diameter (MVD), airspeed and exposure time on the ice formation characteristics as well as the aerodynamic behavior of the NACA 0012 airfoil were investigated using numerical methods. The impact of these parameters was assessed by observing variations in lift and drag values, along with alterations in the shape of the airfoil. To ensure the reliability of the numerical methodology, validation studies were conducted by comparing simulation results for both clean and iced airfoil configurations at various angles of attack with experimental data available in the literature. Analyses of the clean airfoil were performed using ANSYS Fluent, while ice accretion analyses were carried out with the FENSAP-ICE software employing the Spalart-Allmaras turbulence model. Results show that increasing AoA leads to asymmetric ice horn growth and up to 56% lift loss and 625% drag increase at 12°. An increase in liquid water content caused the ice structure to become more irregular and expanded the ice-covered area on both the upper and lower surfaces. As the mean volumetric diameter increased, ice formation spread over a larger area; notably, at an MVD of 50 µm, the highest performance losses were observed despite the maximum ice thickness not occurring at this value. With increasing airspeed, the ice shapes became sharper and more pronounced, and aerodynamic degradation was more significant especially up to speeds of 90 m/s. Finally, longer exposure times caused an increase in both ice thickness and the extent of the ice-covered area, with maximum ice accretion observed after 8 minutes. These findings demonstrate that each parameter significantly affects not only ice geometry but also the aerodynamic performance, which is critical for flight safety.

Keywords: NACA 0012, Ice accretion, CFD, FENSAP-ICE

ÖZET

SAYISAL METOTLAR İLE UÇAK KANATLARINDAKİ BUZLANMA MEKANİZMASININ İNCELENMESİ

ONAY, CEM

MAKİNE MÜHENDİSLİĞİ YÜKSEK LİSANS TEZİ

Danışman: Doç. Dr. Ülkü Ece AYLI
Ortak Danışman: Dr. Öğr. Üyesi Eyup KOÇAK
Eylül 2025, 82 Sayfa

Bu tez çalışmasında; hücum açısı, sıvı su içeriği (LWC), ortalama damla çapı (MVD), uçuş hızı ve buzlanma süresi gibi temel parametrelerin, NACA 0012 kanat profili üzerindeki buz oluşum karakteristikleri ve aerodinamik davranış üzerindeki etkileri sayısal yöntemler kullanılarak incelenmiştir. Bu parametrelerin etkileri, kaldırma ve sürükleme katsayılarındaki değişimler ile kanat geometrisindeki şekil bozulmaları gözlemlenerek değerlendirilmiştir. Sayısal yöntemin güvenilirliğini sağlamak amacıyla, farklı hücum açıları altında temiz ve buzlu kanat profilleri için yapılan simülasyon sonuçları, literatürdeki deneysel verilerle karşılaştırılarak doğrulama çalışmaları gerçekleştirilmiştir. Temiz kanat analizleri ANSYS Fluent yazılımı ile, buzlanma analizleri ise FENSAP-ICE programı kullanılarak ve Spalart-Allmaras türbülans modeli ile gerçekleştirilmiştir. Sonuçlar, hücum açısının artmasının asimetrik buz boynuzu büyümesine yol açtığını ve 12° hücum açısında kaldırma katsayısında %56'ya varan azalma ile sürükleme katsayısında %625'e varan artışa neden olduğunu göstermiştir. Sıvı su içeriğinin yükselmesi, buz yapısının daha düzensiz hale gelmesine ve hem üst hem de alt yüzeyde buz kaplı alanın genişlemesine neden olmuştur. Ortalama damla çapı arttıkça buz oluşumu daha geniş bir yüzeye yayılmış; özellikle 50 µm değerinde, maksimum buz kalınlığı gözlemlenmemesine rağmen en yüksek performans kayıpları tespit edilmiştir. Uçuş hızı arttıkça buz şekli daha keskin ve belirgin hale gelmiş; özellikle 90 m/s’ye kadar olan hızlarda aerodinamik bozulmaların daha fazla olduğu görülmüştür. Son olarak, daha uzun maruz kalma süreleri hem buz kalınlığında hem de buzla kaplı alanın genişliğinde artışa neden olmuş olup, maksimum buz birikimi 8 dakika sonunda gözlemlenmiştir. Bu bulgular, incelenen her bir parametrenin sadece buz geometrisini değil, aynı zamanda uçuş güvenliği açısından kritik öneme sahip aerodinamik performansı da önemli ölçüde etkilediğini ortaya koymaktadır.

Anahtar Kelimeler: NACA 0012, Buzlanma, HAD, FENSAP-ICE

ACKNOWLEDGEMENT

I would like to express my deepest gratitude to my supervisor, Assoc. Prof. Dr. Ülkü Ece Aylı, for her invaluable guidance, support, and encouragement throughout this research. I also extend my sincere thanks to Assist. Prof. Dr. Eyup Kocak for his helpful guidance and constructive feedback during the thesis process.

I am truly grateful to my mother Cahide Onay and my father Necmi Onay, for their endless love and unconditional support throughout my academic journey.

I am also thankful to my grandmothers Ayşe Erikçi and Meşkure Onay for encouraging me with their prayers whenever I needed strength.

TABLE OF CONTENTS

LIST OF TABLE

LIST OF FIGURES

LIST OF SYMBOLS AND ABBREVIATIONS

SYMBOLS

Cl	: Lift Coefficient
Cd	: Drag Coefficient
ρ	: Density
σ^{ij}	: Stress Tensor
τ^{ij}	: Shear Stress
κ	: Thermal Conductivity
$\vec{g}$	: Gravity Vector
ν	: Kinematic Viscosity
c	: Chord Length
T_s	: Static Temperature
Re_d	: Droplets Reynolds Number
K	: Inertial Parameter
Fr	: Froude Number
C_D	: Droplet Drag Coefficient
h_f	: Film Thickness
$\dot{m}_{ice}$	: Instantaneous Mass Accumulation of Ice

ABBREVIATIONS

CFD	: Computational Fluid Dynamics
RANS	: Reynolds Averaged Navier – Stokes
SLD	: Supercooled Large Droplet
NTSB	: The National Transportation Safety Board
LWC	: Liquid Water Content
MVD	: Median Volumetric Diameter
AoA	: Angle of Attack
NASA	: National Aeronautics and Space Administration

CHAPTER I

1. INTRODUCTION

Flight safety is one of the most critical aspects of modern aviation, and atmospheric icing remains one of the most significant hazards to aircraft operations. Aircraft icing denotes the accumulation of frozen water on the aircraft structure, particularly on surfaces directly exposed to the airflow, such as the wings, engine inlets, and tail. This process happens when supercooled water droplets strike the aircraft surfaces and freeze upon contact under sub-zero conditions. Narrow and sharp-edged components tend to collect droplets more readily and initiate rapid ice formation. Consequently, icing is most commonly observed on slender regions such as the leading edges of the wings. A visual representation of ice formation on aircraft wings is provided in Figure 1.1.

Figure 1.1: Ice accretion on an aircraft wing [1]

Icing on aircraft wings significantly degrades aerodynamic performance, with the severity depending on the type, location, and thickness of the ice. The accumulated ice can form in various shapes and layers, altering the wing's geometry, which in turn reduces lift and increases drag.

The effect of icing on the lift coefficient (Cl) and drag coefficient (Cd) can be seen more clearly with the graphs. The Figure 1.2 shows how ice formation on wing negatively affect the lift coefficient in comparison to a clean airfoil.

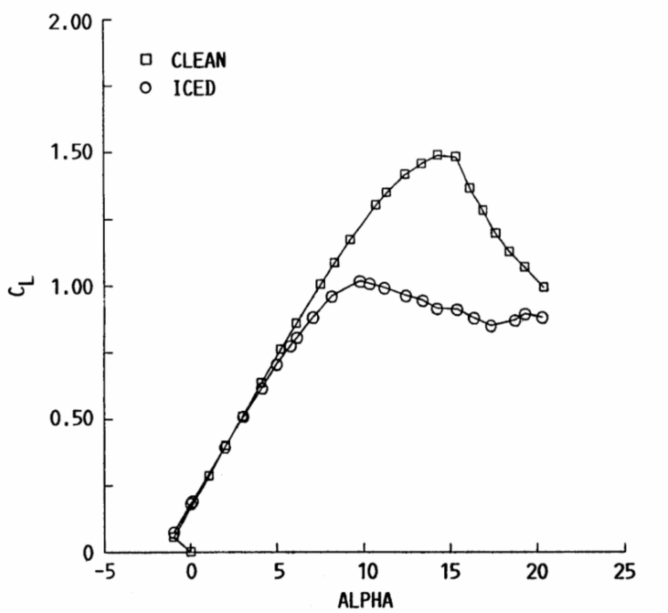

Figure 1.2: Effect of ice accretion on lift [2]

Similarly, the Figure 1.3 shows the effect of ice accumulation on the drag coefficient compared to a clean airfoil.

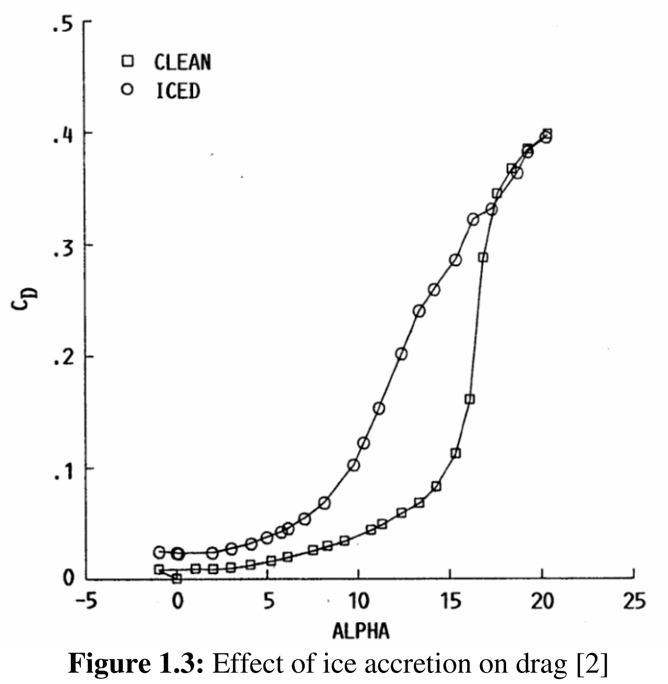

Figure 1.3: Effect of ice accretion on drag [2]

1.1 AIRCRAFT ICING ACCIDENTS

Despite the advancing technology, accidents caused by icing are still a significant issue for the industry. The additional weight and drag caused by ice accumulation can increase the aircraft's fuel consumption and also makes it difficult to maintain altitude and control. Additionally, ice formation on the wings can disrupt airflow and cause loss of lift as it distorts the wing geometry, causing the aircraft to stall at lower angles of attack.

According to the Air Safety Foundation, a total of 3,230 weather aircraft accidents were reported between 1990 and 2000, and 12% of these were related to icing. Of these icing-related accidents, 8% were caused by ground accumulation, 40% by structural icing, and 52% by induction icing [3].

The Roselawn ATR-72 accident is one of the most important icing-related crashes in aviation history. This tragic accident occurred on October 31, 1994, resulting in the deaths of 68 people. The National Transportation Safety Board (NTSB) found that the crash was caused by a sudden loss of control due to ice accretion behind the deice boots on the wing. After this accident, research on icing aerodynamics accelerated significantly. Especially, studies on ice shapes formed in Supercooled Large Droplet (SLD) conditions became more important [4,5].

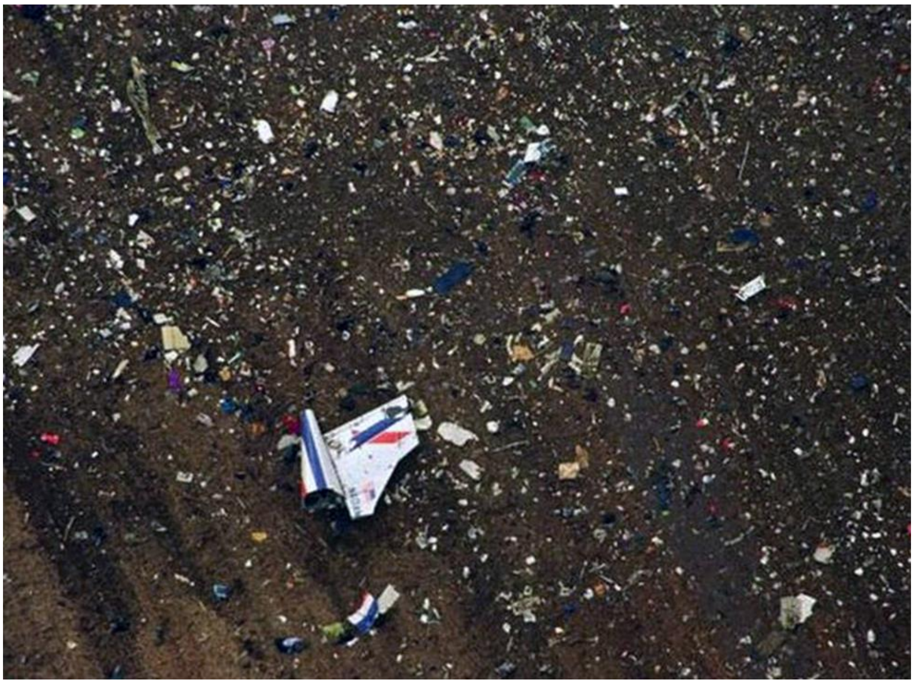

Figure 1.4: The Roselawn ATR-72 accident [6]

1.2 TYPES OF ICING

Ice can accumulate on aircraft surfaces through various mechanisms. The most commonly observed types of aircraft icing are categorized into three main forms: glaze, rime, and mixed icing.

1.2.1 Glaze Ice

Glaze ice, as shown in Figure 1.5, usually forms when the temperature is close to 0°C and the droplets are large. Glaze ice formation is more commonly observed at high liquid water content (LWC). It has irregular shape and transparent, glassy appearance. Furthermore, it is more difficult to detect visually than the rime ice type and has more aerodynamic disadvantages. It forms at higher temperatures than the rime ice type. (0 °C to –10 °C) [7].

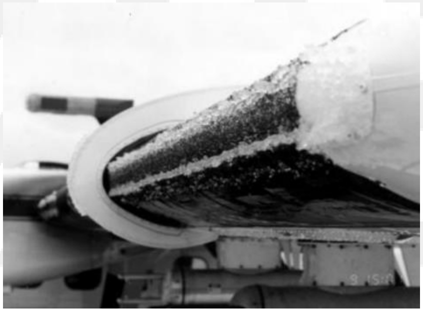

Figure 1.5: Glaze Ice [8]

1.2.2 Rime Ice

Figure 1.6 shows the formation of rime ice, which usually occurs at low temperatures and when the droplets are small. It generally forms at low liquid water content. Unlike glaze ice, it has white matte and opaque appearance. Since its shape fit to the airfoil leading edge, it has less aerodynamics disadvantages. It generally tends to occur at temperatures –15 °C to –40 °C [7].

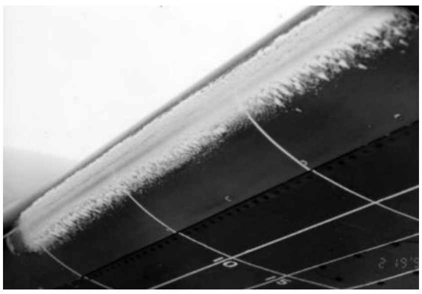

Figure 1.6: Rime Ice [8]

1.2.3 Mixed Ice

Mixed ice, as illustrated in Figure 1.7, can be considered a combination of glaze and rime ice. It may have an irregular shape like glaze ice, but visually, it is closer to the rime ice type. It has an impact on aerodynamic performance similar to glaze and rime ice types, and this must be taken into consideration. It generally forms between temperatures of -10 °C and -15 °C. [7].

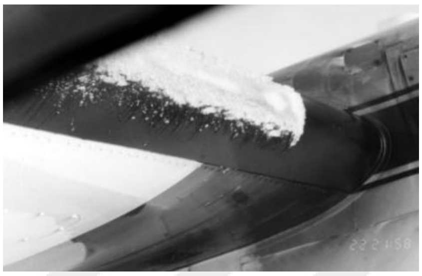

Figure 1.7: Mixed Ice [8]

To facilitate a clearer understanding of the distinct characteristics of glaze and rime ice, a simplified comparison is presented in the table below. This comparison highlights key differences in their formation mechanisms and physical properties, providing a concise overview for better interpretation of their impact on aircraft performance.

Table 1.1: Differences between glaze ice and rime ice

	Glaze Ice	**Rime Ice**
Appearance	Transparent, glassy	White, matte and opaque
LWC	High	Low
MVD	High	Low
Temperature	0 °C to –10 °C	–15 °C to –40 °C
Shape	Irregular	Mostly regular

1.3 MAIN PARAMETERS AFFECTING AIRCRAFT ICING

Understanding the parameters that influence ice formation on aircraft surfaces is essential for predicting aerodynamic degradation and for developing effective anti-icing strategies. The severity and characteristics of ice accretion are governed by a complex interplay of environmental and operational conditions. In the following sections, the effects of key parameters, namely temperature, liquid water content (LWC), median volumetric diameter (MVD), airspeed, and ice accretion time, on the type, extent, and aerodynamic impact of icing are examined in detail, supported by experimental and graphical findings from the literature.

1.3.1 Temperature

The formation of ice on aircraft wings is significantly impacted by temperature. The impact of temperature changes on ice formations under two separate icing conditions is presented in Figure 1.8. It is clearly observed that as the temperature increases, the ice accumulation on the surface decreases. Additionally, at lower temperatures the ice type is rime, while as the temperature increases, the icing pattern becomes more irregular and transforms into glaze ice [9].

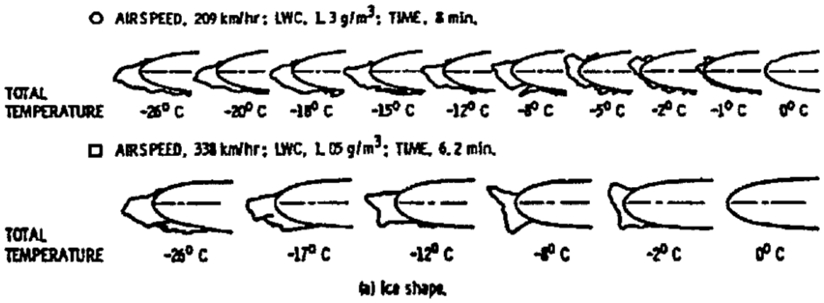

Figure 1.8: The effect of temperature on ice formation [9]

The variation of the drag coefficient with temperature is shown in Figure 1.9. As seen, the drag coefficient reaches its highest levels at around -5 °C, where the icing pattern is the most irregular and has the greatest aerodynamic disadvantages. It can also be seen from this graph that a relatively small change in temperature may be enough to transition to a glaze ice type, which significantly increases drag coefficient [9].

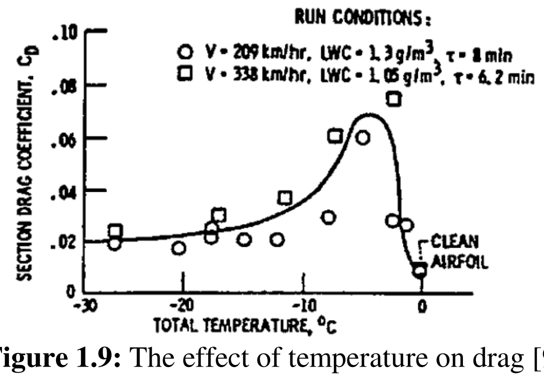

Figure 1.9: The effect of temperature on drag [9]

1.3.2 Liquid Water Content

Liquid water content (LWC) refers to the amount of water mass present in a cloud per unit volume of dry air, typically expressed in grams per cubic meter (g/m^3).

Figure 1.10 illustrates the ice formations resulting from changes in LWC values under two different temperature cases. It can be seen that as the LWC increases, icing on the leading edges of the airfoils increases in both conditions [9].

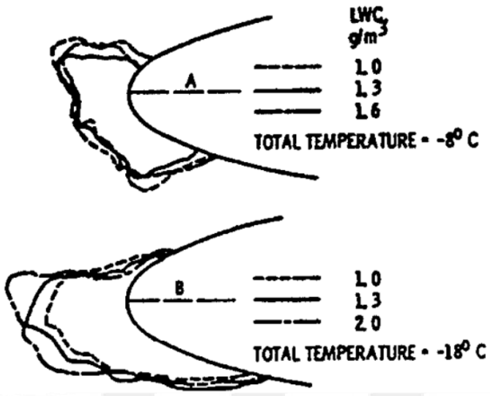

Figure 1.10: The effect of LWC on ice formation [9]

The effect of LWC variation on the drag coefficient under two different icing cases is presented in Figure 1.11. In both cases, an increase in LWC resulted in a corresponding rise in the drag coefficient. Notably, this effect is more pronounced under glaze icing conditions, where the increase in LWC led to a substantial deterioration in aerodynamic performance.

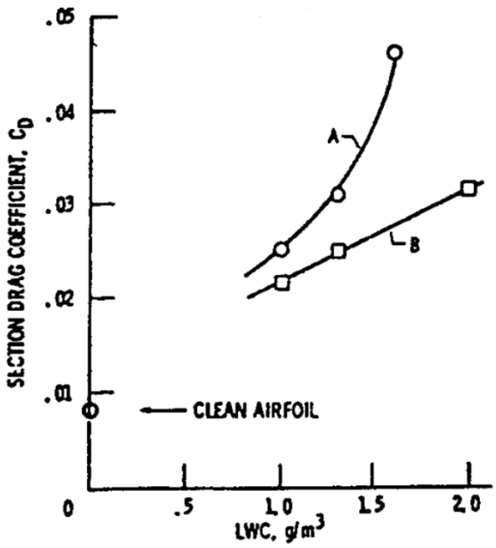

Figure 1.11: The effect of LWC on drag [9]

1.3.3 Median Volumetric Diameter

The size of liquid water droplets is typically expressed in terms of the median volumetric diameter (MVD), and its unit is micrometers. Figure 1.12 shows ice shapes obtained only by increasing the MVD under different icing conditions. As expected, the increase in MVD led to an increase in the amount of icing in all cases [9].

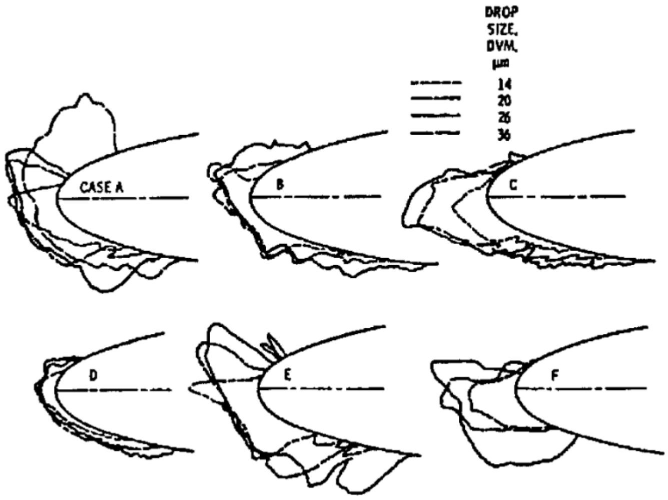

Figure 1.12: The effect of MVD on ice formation [9]

1.3.4 Airspeed

One of the important factors influencing ice accretion on aircraft is airspeed. With increasing airspeed, the water droplets have less time to escape from the surface, which results in greater ice accumulation on the wing surface.

Figure 1.13 illustrates the ice formations observed at three different airspeeds, along with the corresponding changes in drag coefficient under each condition [9].

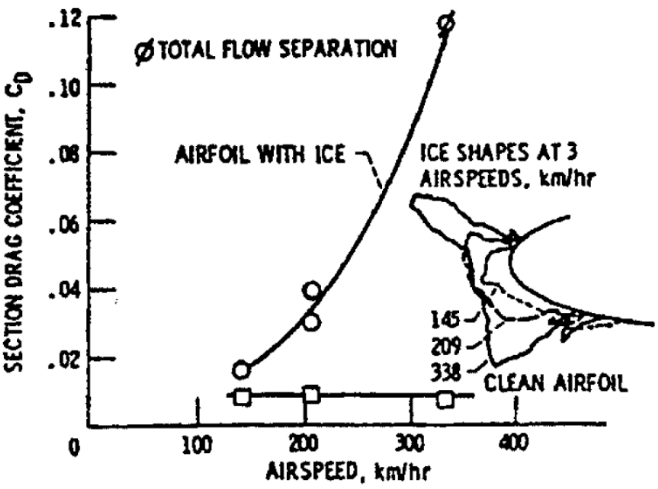

Figure 1.13: The effect of Airspeed on ice formation and drag [9]

It can be seen that as the airspeed increases, ice accumulation on the wings also increases. Moreover, the most irregular ice shape is occurred at 338 km/hr and this proves to us that irregular ice shapes and glaze type of icing are more prominently observed at higher speeds [9].

1.3.5 Ice Accretion Time

As shown in Figure 1.14, cases A, B, and C show the effects of 2, 5 and 15-minute icing durations under glaze ice conditions for different angle of attack values. Similarly, cases D, E, and F show the effects of the same icing durations under rime ice conditions at different angle of attack values. It is observed that in all cases, ice accumulation increased as the icing duration increased [9].

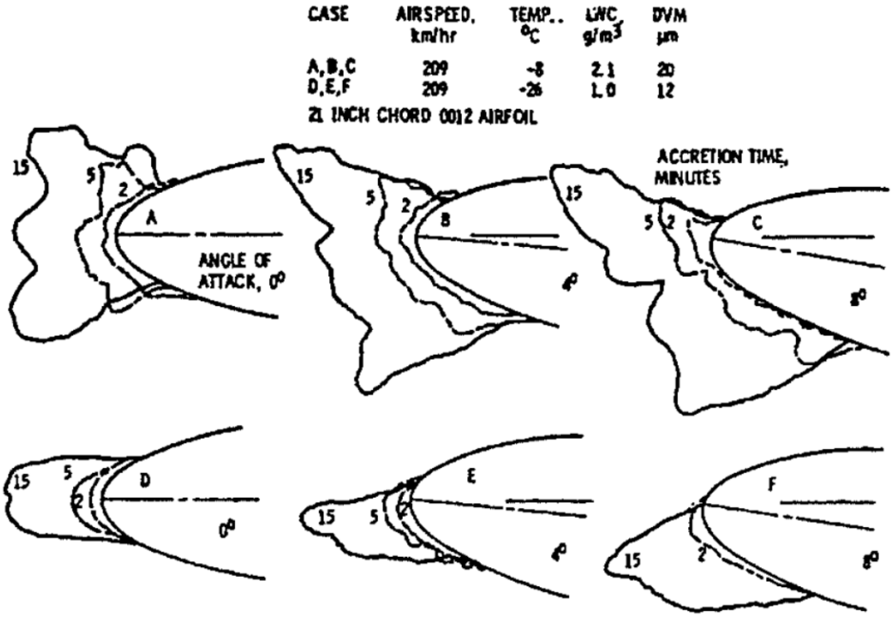

Figure 1.14: The effect of time on ice formation [9]

1.4 AIRCRAFT ICE PROTECTION SYSTEMS

Aircraft icing is a critical phenomenon that must be either prevented or eliminated once it occurs. To address this issue, two primary strategies are employed: anti-icing and de-icing systems. Anti-icing systems are designed to prevent the formation of ice on critical surfaces, whereas de-icing systems function to remove ice that has already accumulated on the aircraft.

1.4.1 Pneumatic Boot De-Icing Systems

This de-icing method is intended to remove ice after it has accumulated on the airfoil, meaning it is not used to prevent ice accumulation. Basically, it removes ice accumulations by inflating and deflating tubes mechanically placed on the surface.

Inflation of the tubes breaks up the ice on the surface and allows it to be removed. Figure 1.15 shows the spanwise and chordwise configurations of pneumatic boots. The tubes can be arranged either spanwise or chordwise, but the more commonly used design is one with tubes arranged spanwise. For pneumatic boots to work efficiently, they need to inflate and deflate quickly. To achieve this, the time required to reach full pressure should be approximately 5 to 6 seconds. For moderate icing conditions, a 60-second cycle is recommended, while in lighter icing conditions, longer ice accumulation times of 3-4 minutes can be acceptable [10].

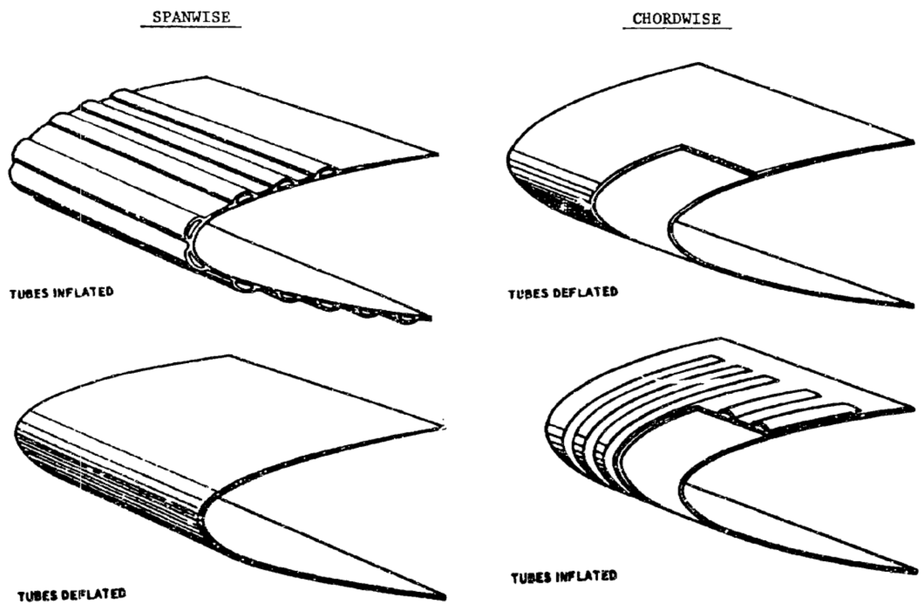

Figure 1.15: Pneumatic Boot De-Icing system [10]

1.4.2 Electro-Thermal Systems

Another ice protection system is electro thermal system as shown in Figure 1.16. These systems are divided into two as anti-icing and de-icing systems. Electro-thermal systems utilize electrical heaters to keep the surface temperature above freezing during icing conditions or to quickly apply heat to the surface after ice has formed. In order for these systems to operate, an energy source, a cabling system to distribute the energy, resistance heaters and control system are required [10].

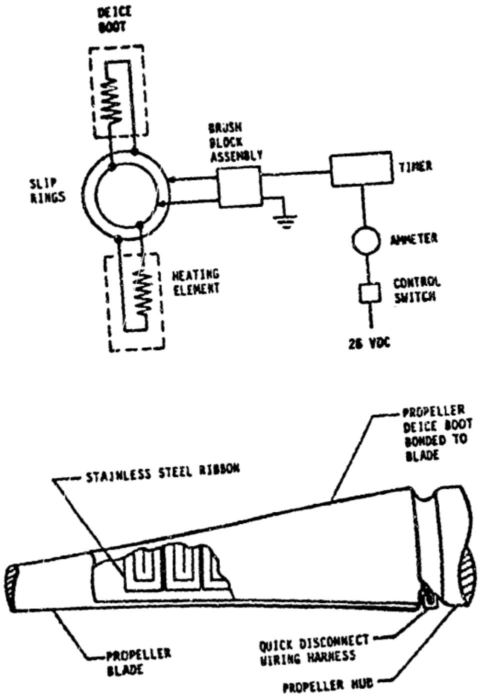

Figure 1.16: Electro-Thermal De-Icing system [10]

1.4.3 Fluid Ice Protection Systems

Fluid ice protection systems work by coating the surface to be protected from icing with a fluid that lowers its freezing point. These fluids are referred to as freezing point depressant (FPD). When supercooled water droplets come into contact with a surface, they mix with the FPD, forming a mixture that has a freezing point lower than the ambient air temperature. This mixture eventually evaporates or is released from the surface. While there are several chemicals that lower the freezing point of water when mixed with it, the most commonly used substances for de-icing or anti-icing operations are glycol and alcohol. The freezing point of glycol is approximately -12 °C, but when combined with an equal volume of water, depending on the type of glycol used, it can drop to between -22 °C and -40 °C [10].

1.4.4 Electro-Impulse De-Icing Systems

It is a mechanical de-icing system, similar to the pneumatic boot de-icing system. Figure 1.17 shows a cross-section of the Electro-Impulse system. A sudden high voltage (typically 800 to 1400 V) is passed through the coils placed under the surface where the ice will be removed, and the resulting pulsed movement is aimed at removing the ice. The peak force on the surface is in the range of 1780-2220 Newtons. Since it does not disrupt the airflow, it does not have a negative effect on aerodynamic performance. Low power requirement is one of the most important factors that make this system advantageous [10].

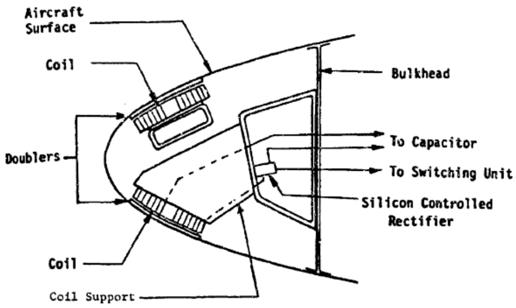

Figure 1.17: Impulse Coils located at the leading edge [10]

1.4.5 Hot Air Systems

Similar to electro-thermal systems, it can also be applied for anti-icing and de-icing applications. The basic principle of this system is to heat the surfaces that are either already iced or need to be protected from icing by using a hot air source. Potential hot air sources include engine compressor air, shaft-driven compressors, exhaust gases, or fuel-burning combustion heaters [10].

1.5 LITERATURE SURVEY

A detailed review of the available studies is necessary to understand the current knowledge of research on aircraft icing phenomena, its aerodynamic implications, and the effectiveness of various mitigation strategies. Numerous experimental, numerical, and analytical studies have been conducted to investigate ice formation mechanisms, classify icing types, and assess their impact on aircraft performance. This section summarizes key contributions in the literature, highlighting the methodologies, findings, and knowledge gaps relevant to the present study.

Aircraft icing has been an important research topic since the early years of aviation and remains a significant issue today. The studies by Hardy (1946) [11], Langmuir & Blodgett (1946) [12] and Messinger (1953) [13] contributed to the development of the first mathematical models and laid the foundation for later research [14].

Institutions such as NASA’s Lewis Research Center, the Office National d'Études et de Recherches Aérospatiales (ONERA), and the Royal Aerospace Establishment (RAE) have led research on aircraft icing. Especially during World War

II, there was a need for specialized icing wind tunnels to experimentally investigate ice accumulation on aircraft surfaces. These icing wind tunnels were built to simulate the atmospheric conditions encountered during flight in a laboratory environment. In this way, ice formation on aircraft wings and other surfaces under certain atmospheric conditions was tested. These tests provided critical data for understanding the mechanisms of ice formation, determining its effects on aerodynamic performance, and developing effective anti-icing and de-icing systems.

Since the 1980s, NASA has been conducting both numerical and experimental research on aircraft icing. While experimental research has been carried out at NASA's Glenn Icing Research Tunnel, the LEWICE software, developed by the same institution, has become one of the most widely used and reliable tools for numerical icing analyses. Numerous reports based on these experiments and simulations have been published, becoming key references for researchers working on aircraft icing in the literature. In particular, icing studies on the NACA 0012 airfoil serve as primary sources for validation studies.

Notable research on NACA 0012 airfoil icing has been carried out by Olsen et al. [15], Shin and Bond [16], and Wright et al. [17]. These studies investigated how various factors such as temperature, airspeed, mean volume diameter (MVD), and liquid water content (LWC) affect ice accumulation.

Lee and Bragg [18] carried out experiments to analyze the aerodynamic effects of simulated supercooled large droplet ice accumulation on a modified NACA 23012 airfoil. The study was conducted at a Reynolds number of 1.8×10^6 and the effects of the positions of different ice shapes on lift, drag and pitching moments were examined. Their findings showed that the placement of ice shapes significantly changes the aerodynamic performance of the airfoil. The study further shows that the most critical location for ice accretion, in terms of lift reduction, was at 12% chord, with a height-to-chord ratio of 0.0139. At this location, the maximum lift coefficient decreased significantly to 0.27, compared to 1.46 for the clean airfoil.

In a study conducted by Kim and Bragg [19], the aerodynamic effects of simulated ice shape geometries on a flapped NLF(1)-0414 airfoil were investigated through wind tunnel experiments. The ice shapes were fabricated from aluminum in three different sizes and positioned at six distinct surface locations on the airfoil. The tests were conducted at three Reynolds numbers: 0.5, 1.0 and 1.8×10^6. The results revealed an almost linear correlation between the loss in maximum lift and the location of the ice horn, with the most significant degradation observed when the ice was placed furthest along the upper surface. Additionally, the study concluded that variations in Reynolds number had minimal influence on the overall aerodynamic performance of the airfoil.

Broeren et al. [20] conducted an experimental study to analyze the aerodynamic performance penalties of a 36-inch chord NACA 23012 airfoil under various icing conditions, selected based on the FAR 25 Appendix C. The tests were carried out at static air temperatures of −22 °F, −4 °F, 14 °F, and 21 °F. Cloud droplet median volumetric diameters of 20 μm and 40 μm were used, while cloud liquid water content ranged from 0.15 to 2.20 g/m^3 to represent various icing scenarios. The simulated intercycle ice shapes caused a marked reduction in the aerodynamic performance of the airfoil. The lift coefficient dropped significantly, by approximately 60%, going from 1.8 to 0.7. The stall angle also reduced, falling from 17° in clean conditions to 9° when ice was present. Additionally, the minimum drag coefficient rose from 0.007 to 0.026. Moreover, variations in Reynolds and Mach numbers had little effect on the performance coefficients of the iced airfoil.

Chi et al. [21] performed a study using CFD tools such as WIND, Fluent, and PowerFLOW to predict the lift, drag, and moment coefficients of a business-jet airfoil (GLC305) with rime and glaze ice accretions. In the study, various turbulence models, such as Spalart-Allmaras, RNG k-ϵ, shear-stress transport, v^2-f and differential Reynolds stress models were evaluated by comparing their results with experimental data. The results obtained are presented in graphical form.

Son et al. [22] developed a code to predict ice shape formation on a two-dimensional airfoil. The developed code was compared with existing ice accretion analysis codes under three different conditions: rime, mixture, and glaze. Parameters such as the cross-sectional area of the ice, maximum ice thickness, ice heading, and distribution of ice thickness were used for comparison. Validations were carried out on the NACA 0012 airfoil. Additionally, ice shapes were determined according to different environmental conditions. The selected environmental parameters included freestream velocity, liquid water content and temperature. The results showed that an increase in LWC led to an increase in the ice accretion area, and a linear correlation was observed between LWC and the ice cross sectional area.

Pouryoussefi et al. [23] conducted an experimental study to investigate the aerodynamic performance penalties of a NACA 23012 airfoil under runback ice, horn ice and spanwise ridge ice conditions at a Reynolds number of 0.6 x 10^6. Tests were performed at angles of attack ranging from −8° to 20°, and the results were compared. Their study showed that spanwise ridge ice had the most significant negative impact on the aerodynamic performance of the airfoil, causing the stall angle drops approximately 10° and the maximum lift coefficient decreased by about 50%. In contrast, runback ice had the least negative effect, with the stall angle decreasing by around 2° and the maximum lift coefficient decreased by approximately 8%.

Sznajder et al. [24] performed ice accretion analyses on the NACA 0012 airfoil using ANSYS software. The simulations were carried out at a Mach number of 0.3, a Reynolds number of 4.39 million and an air temperature of 262 K (-11 °C). In addition, the airfoil was modeled by solving URANS equations with Spalart-Allmaras turbulence model. In this study, they observed a significant decrease in the lift exceeding 50% of the lift produced by the clean airfoil at angle of attack approximately 8 degrees as a result of 420 seconds of simulated ice accretion.

Lu et al. [25] performed ice accretion analyses on the NACA 0012 airfoil by considering various icing durations and different airflow velocities. Simulations were performed at angles of attack of 4°, 8°, 12°, 16° and 20°, and results were compared. In their study, they used ANSYS Fluent software for the airflow field solver and FENSAP-ICE software for the ice accretion solver. Their findings showed that between 0 and 30 minutes, the lift coefficient of an airfoil decreased by up to 48% and 46.2% at angles of attack of 8° and 12°, respectively.

Bhatia and Wahaibi [26] conducted numerical icing simulations on the NACA 23012 airfoil for three different icing scenarios. Analyses were carried out in ANSYS Fluent software with using the SST k-ω turbulence model. According to the results of the study, it was observed that the lift coefficient decreased by up to 75.3% and the drag coefficient increased by up to 280%. In addition, study showed that aerodynamic performance loss is significantly affected by the ridge height, the extent of ice accretion and the thickness of the ice.

Yirtici et al. [27] conducted a study to assess the performance losses caused by icing in wind turbines. In the study, NACA 64618 and S809 airfoils were used for icing validation studies and results observed to be compatible with numerical and experimental studies in the literature. Furthermore, study successfully simulated 24% power loss for 30 kW wind turbine under icing conditions.

Krøgenes et al. [28] performed experimental and numerical analyses using the NREL S826 airfoil to demonstrate aerodynamic performance penalties under rime, glaze and mixed ice cases. The experiments were conducted on an airfoil with 3D-printed ice shapes at a Reynolds number of 1 x 10^5 to 4 x 10^5. According to their study, mixed ice condition had the most significant negative effect on the aerodynamic performance of the airfoil. Under mixed ice condition, lift was reduced by 30% and drag was increased by 340% compared to clean case.

Hann et al. [29] examined the impact of 3D-printed ice formations on the aerodynamic efficiency of an S826 airfoil. Experiments were carried out at three Reynolds numbers (2, 4, and 6 x 10^5). Numerical simulations performed at FENSAP software with using the Spalart Allmaras and Menter's k-ω SST turbulence models. Experimental studies were compared with numerical studies and presented in graphical form. According to the study, it was revealed that rough, rugged, and complex geometries have a more negative impact on aerodynamic performance.

In a study conducted by Hann and Johansen [30], the effects of icing on unmanned aerial vehicles (UAVs) investigated with using FENSAP-ICE software. Their study primarily focused on the effects of airspeed and chord length on ice accretion. The investigations were carried out using the RG-15 airfoil under three icing conditions: glaze, rime, and mixed ice. In their study, the effect of chord length was examined by testing four different chord sizes (0.11 m, 0.23 m, 0.45 m and 0.90 m) at a constant airspeed of 25 m/s. Additionally, the effect of airspeed was examined at four different velocities (12.5 m/s, 25 m/s, 50 m/s and 100 m/s) with a fixed chord length of 0.45 m. The study showed that an increase in airspeed resulted in greater aerodynamic performance penalties. Furthermore, a decrease in chord length also led to more aerodynamic degradation.

Fajt et al. [31] investigated the performance penalties of UAVs under various icing conditions. Numerical analyses were conducted on RG-15 airfoil with using FENSAP-ICE software and validated with experimental data. The study was conducted at a constant airspeed of 25 m/s. Median volumetric diameter values of 15 μm, 20 μm, 30 μm, and 40 μm were selected and for each MVD, the effects of temperatures at –2 °C, –5 °C, –15 °C, and –30 °C were examined. According to the results of their studies, they found that lift could decrease by up to 35% and drag could increase by up to 160% under icing conditions.

1.6 OBJECTIVE OF THE THESIS

The primary objective of this thesis is to investigate the effects of key atmospheric and operational parameters, namely Liquid Water Content (LWC), Median Volumetric Diameter (MVD), airspeed and exposure time on ice accretion characteristics and aerodynamic performance of an airfoil. To ensure the reliability of the numerical methodology, initial validation studies were conducted for both clean and iced airfoil configurations under various angles of attack by comparing the simulation results with available experimental data in the literature.

Following the validation phase, a comprehensive parametric study was performed using a verified numerical setup to analyze how variations in LWC, MVD, airspeed and exposure time influence ice shape development and the corresponding aerodynamic degradation. The effects were assessed in terms of changes in lift and drag coefficients, as well as geometric alterations to the airfoil surface under icing conditions.

This study stands out in the literature due to its integrated approach that combines thorough validation, detailed parametric evaluation, and focus on aerodynamic performance at multiple angles of attack. It provides novel insights into how specific icing parameters influence both the severity and aerodynamic consequences of ice accretion, making it one of the few studies in the field that systematically addresses these interactions under controlled numerical conditions.

CHAPTER II

2. NUMERICAL METHODOLOGY

In this study, clean case simulations were performed using the ANSYS FLUENT software. ANSYS FLUENT is a widely used computational fluid dynamics (CFD) tool that numerically solves the Reynolds-Averaged Navier-Stokes (RANS) equations for fluid flow problems. On the other hand, iced case simulation studies were conducted using the FENSAP-ICE software. In order to simulate ice accretion on the airfoil surface, firstly a flow field solution is required, secondly, droplet trajectory prediction is needed to determine impingement locations of water droplets on the surface, and finally, an ice accretion tool is required to perform heat transfer calculations for evaluating ice growth.

As defined in the study by Cao et al. [32], the following fundamental assumptions are made for the governing equations of two-phase flows:

- The effect of droplet motion on the airflow is neglected, meaning the volume fraction of the droplets is assumed to be negligibly small.
- Only drag force, gravity, and buoyancy act on the droplets; they are assumed to be unaffected by turbulence-induced fluctuations.
- No heat transfer or evaporation occurs for the droplets, meaning their physical properties remain unchanged.
- All droplets are considered to be spheres with a constant diameter.
- Collision between droplets is ignored.
- After impacting the wing surface, the droplets do not bounce or splash.

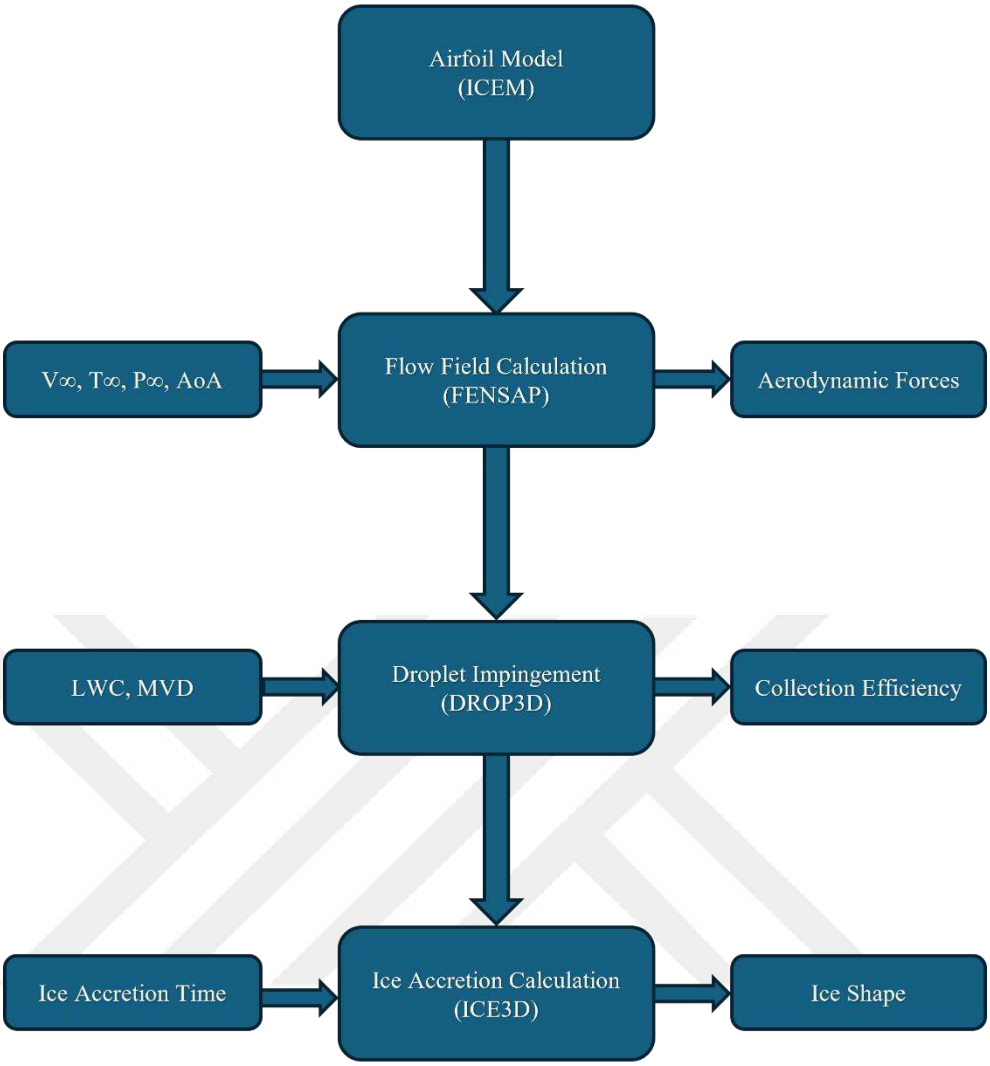

Figure 2.1: Workflow of airfoil icing simulation

2.1 FLOW FIELD CALCULATIONS

For droplet trajectory and ice accretion simulations, the flow field solution is obtained through FENSAP module within the FENSAP-ICE software. Similar to the FLUENT, FENSAP also solves the Reynolds-Averaged Navier-Stokes (RANS) equations to determine the flow field characteristics. The flow field is modeled using partial differential equations that represent the conservation of mass, momentum, and energy [33].

2.1.1 Governing Equations

The continuity equation is presented in Equation 2.1 as follows:

$$\frac{\partial \rho_a}{\partial t} + \vec{\nabla} \cdot \left(\rho_a \vec{V_a}\right) = 0 \tag{2.1}$$

In the equation, ρ denotes the density V is the velocity vector, t is the time, subscript a refers to air solution.

The momentum equation is presented in Equation 2.2 as follows:

$$\frac{\partial(\rho_a \vec{V}_a)}{\partial \mathrm{t}} + \vec{\nabla} \cdot (\rho_a \vec{V}_a \vec{V}_a) = \vec{\nabla} \cdot \sigma^{ij} + \rho_a \vec{g} \tag{2.2}$$

Where σ^{ij} is the stress tensor and is presented in Equation 2.3 as follows:

$$\sigma^{ij} = -\delta^{ij} p_a + \tau^{ij} \tag{2.3}$$

In the Equation, p is the static pressure and τ^{ij} is shear stress.

The energy equation is presented in Equation 2.4 as follows:

$$\frac{\partial \rho_a E_a}{\partial t} + \vec{\nabla} \cdot (\rho_a \vec{V}_a H_a) = \vec{\nabla} \cdot \left(\kappa_a (\vec{\nabla} T_a) + v_i \tau^{ij}\right) + \rho_a \vec{g} \cdot \vec{V}_a \tag{2.4}$$

In the equation, E and H are the total internal energy and enthalpy, κ is the thermal conductiviy and $\vec{g}$ is the gravity vector [33].

2.1.2 Spalart Allmaras Turbulence Model

The Spalart-Allmaras model is a one-equation turbulence model and was used in the analyses [33].

$$\mu_T = \tilde{\nu} f_{v1} \tag{2.5}$$

Where $\tilde{\nu}$ is determined through the transport equation, as given in Equation 2.6.

$$\frac{\partial \tilde{\nu}}{\partial t} + u_j \frac{\partial \tilde{\nu}}{\partial x_j} = c_{b1} \tilde{S} \tilde{\nu} + \frac{1}{\sigma \mathrm{Re}_\infty} \frac{\partial}{\partial x_k} \left[(\nu + \tilde{\nu}) \frac{\partial \tilde{\nu}}{\partial x_k} + \frac{\partial \tilde{\nu}}{\partial x_k} \frac{\partial \tilde{\nu}}{\partial x_k} \right] - c_{w1} f_w \frac{1}{\mathrm{Re}_\infty} \left(\frac{\tilde{\nu}}{d} \right)^2 \tag{2.6}$$

$$\tilde{S} = S + \frac{1}{\mathrm{Re}_\infty} \frac{\tilde{\nu}}{\kappa^2 d^2} f_{v2} \tag{2.7}$$

$$S = \sqrt{2\Omega_{ij}\Omega_{ij}} \tag{2.8}$$

$$\Omega_{ij} = \frac{1}{2}\left(\frac{\partial u_i}{\partial x_j} - \frac{\partial u_j}{\partial x_i}\right) \tag{2.9}$$

The variable d represents the distance to the closest wall. The functions f_{v1} and f_{v2} are given in Equations 2.10 and 2.11.

$$f_{v1} = \frac{\chi^3}{\chi^3 + c_{v1}^3} \tag{2.10}$$

$$f_{v2} = 1 - \frac{\chi}{1 + \chi f_{v1}} \tag{2.11}$$

$$\chi = \frac{\tilde{\nu}}{\nu} \tag{2.12}$$

The term ν denotes the laminar kinematic viscosity of the fluid.
The destruction term f_w is calculated based on the following equations.

$$f_w = g\left(\frac{1 + c_{w3}^6}{g^6 + c_{w3}^6}\right)^{\frac{1}{6}} \tag{2.13}$$

$$g = r + c_{w2}(r^6 - r) \tag{2.14}$$

$$r = \frac{\tilde{\nu}}{\kappa^2 d^2 Re_\infty S + \tilde{\nu} f_{v2}} \tag{2.15}$$

2.1.3 Surface Roughness

To simulate the distribution of sand-grain roughness over the airfoil surface, the empirical correlation developed by Shin et al. were applied, as shown in Equation 2.16 [33].

$$k_s = 0.6839\left[\frac{\frac{k_s}{c}}{\left(\frac{k_s}{c}\right)_{\text{base}}}\right]_{LWC}\left[\frac{\frac{k_s}{c}}{\left(\frac{k_s}{c}\right)_{\text{base}}}\right]_{T_s}\left[\frac{\frac{k_s}{c}}{\left(\frac{k_s}{c}\right)_{\text{base}}}\right]_{MVD}\left(\frac{k_s}{c}\right)_{\text{base}} c \qquad (2.16)$$

In Equation 2.16, c represents the airfoil chord, and $\left(\frac{k_s}{c}\right)_{\text{base}}$ is equal to 0.001177. The parameters liquid water content (LWC), static temperature T_s and median volume droplet (MVD) are described respectively by the given equations below [34].

$$\left[\frac{k_s/c}{(k_s/c)_{\text{base}}}\right]_{LWC} = 0.5714 + 0.2457(LWC) + 1.2571(LWC)^2 \qquad (2.17)$$

$$\left[\frac{k_s/c}{(k_s/c)_{\text{base}}}\right]_{T_s} = 0.047T_s - 11.27 \qquad (2.18)$$

$$\left[\frac{k_s/c}{(k_s/c)_{\text{base}}}\right]_{\text{MVD}} = 1 \quad (\text{MVD} \leq 20), \quad 1.667 - 0.0333\,\text{MVD} \quad (\text{MVD} > 20) \qquad (2.19)$$

2.2 DROPLET IMPINGEMENT ANALYSIS

Droplet trajectory prediction and impingement analysis were performed using the DROP3D module of the FENSAP-ICE software. DROP3D computes particle flow as a continuum using the Eulerian approach. The general Eulerian two-fluid model comprises the Euler or Navier-Stokes equations extended by additional equations for droplet continuity and momentum, which are presented in Equations 2.20 and 2.21 [33].

$$\frac{\partial \alpha}{\partial t} + \vec{\nabla} \cdot \left(\alpha \vec{V}_{\text{d}}\right) = 0 \qquad (2.20)$$

In Equation 2.20, α denotes the mean field value of the particle concentration, while V_d represents the mean field value of the particle velocity.

$$\frac{\partial\left(\alpha \vec{V}_d\right)}{\partial t} + \vec{\nabla}\left[\alpha \vec{V}_d \otimes \vec{V}_d\right] = \frac{C_D \text{Re}_d}{24K}\alpha\left(\vec{V}_a - \vec{V}_d\right) + \alpha\left(1 - \frac{\rho_a}{\rho_d}\right)\frac{1}{Fr^2} \qquad (2.21)$$

In Equation 2.21, the first term on the right-hand side denotes the drag acting on particles of mean diameter d.

The droplets Reynolds number Re_d is given in Equation 2.22.

$$\mathrm{Re}_d = \frac{\rho_a\, dV_{a,\infty}||\vec{V}_a - \vec{V}_d||}{\mu_a} \tag{2.22}$$

The inertial parameter K is given in Equation 2.23.

$$K = \frac{\rho_d d^2 V_{a,\infty}}{18 L_\infty \mu_a} \tag{2.23}$$

In Equation 2.21, the second term on the right hand-side expresses buoyancy and gravity forces. It depends on local Froude number.

The local Froude number is given in Equation 2.24.

$$Fr = \frac{||V_{a,\infty}||}{\sqrt{L_\infty g_\infty}} \tag{2.24}$$

C_D is determined using different drag correlations. In this study, the water-default droplet drag model was selected. According to this model, the drag coefficient C_D is calculated based on Equation 2.25 and 2.26.

$$C_D = (24/\mathrm{Re}_d)(1 + 0.15\mathrm{Re}_d^{0.687}) \quad \text{for } \mathrm{Re}_d \leq 1300 \tag{2.25}$$

$$C_D = 0.4 \quad \text{for } \mathrm{Re}_d > 1300 \tag{2.26}$$

The validity range of this drag coefficient is not constrained by Re_d. However, water droplets are generally observed to deform at Re_d values exceeding 250 [33].

2.3 ICE ACCRETION ANALYSIS

Ice accretion analyses were performed using the ICE3D module of the FENSAP-ICE software. In the ICE3D module, the mass balance calculations for icing simulations are based on the Messinger model.

The contamination resulting from impinging droplets is modeled as a thin liquid film on each solid surface. This film may run back under the influence of shear stresses generated by the airflow, gravity, or centrifugal forces. The height of the liquid film must be determined at all grid points on the solid surfaces. Depending on the thermodynamic conditions of the surface, part of the film may freeze (ice accretion), evaporate, or sublimate [33].

The ICE3D module solves a set of two partial differential equations on all solid surfaces. The first equation represents mass conservation and is provided in Equation 2.27.

$$\rho_f \left[\frac{\partial h_f}{\partial t} + \vec{\nabla} \cdot \left(\overline{V}_f h_f\right)\right] = V_\infty LWC\beta - \dot{m}_{evap} - \dot{m}_{ice} \tag{2.27}$$

In Equation 2.27, $\overline{V}_f$ represents the mean velocity obtained by averaging the film velocity across the film thickness. The expression for the mean film velocity is provided in Equation 2.28. On the other hand, the terms defined on the right-hand side of the equation represent, respectively, the mass transfer caused by water droplet impingement, evaporation, and ice accretion.

$$\overline{V}_f(\vec{x}, y) = \frac{1}{h_f}\int_0^{h_f} \vec{V}_f(\vec{x}, y)\, dy = \frac{h_f}{2\mu_f}\vec{\tau}_{a,wall}(\vec{x}) \tag{2.28}$$

In the equation, $\vec{V}_f$ is expressed as a function dependent on the surface coordinates x=(x1,x2) and the normal distance y from the surface. To simplify the problem, a linear profile for the film velocity normal to the wall, with the velocity set to zero at the wall is given in Equation 2.29.

$$\vec{V}_f(\vec{x}, y) = \frac{y}{\mu_f}\vec{\tau}_{a,wall}(\vec{x}) \tag{2.29}$$

The second partial differential equation represents the principle of energy conservation and is provided in equation 2.30.

$$\rho_f \left[\frac{\partial h_f c_f T_f}{\partial t} + \vec{\nabla} \cdot \left(\vec{V}_f h_f c_f T_f\right)\right] = \left(e_d + \frac{1}{2}\overrightarrow{V_d^2}\right) V_\infty LWC\beta - \dot{m}_{evap}\left(L_{evap}\right) + \dot{m}_{ice}\left(L_{fus} - c_{ice}T_{ice}\right) - c_h\left(T_f - T_{rec}\right) + \sigma\varepsilon\left(T_\infty^4 - T_f^4\right) + Q_{anti\text{-}icing} \quad (2.30)$$

Equation 2.30 describes energy transfer resulting from water droplets impingement, evaporation and ice accretion. The final three terms correspond to radiative, convective, and one-dimensional conductive heat fluxes which may be provided by an anti-icing heating device. The parameters ρ_f, c_f, L_{evap}, c_{ice}, L_{fus}, σ, ε correspond to physical properties of water and ice, and can be modified through the user interface. The parameters T_∞, V_∞, and LWC are specified by the user. β, e_d, and V_d representing collection efficiency, droplet energy, and droplet impact velocity, respectively, are provided by DROP3D. The evaporative mass flux m_{evap} is recovered from the convective heat transfer coefficient. h_f is the film thickness, T_f is the equilibrium temperature at the air/water film/ice/wall interface, and $\dot{m}_{ice}$ is the instantaneous mass accumulation of ice. These three unknowns need to be computed as part of the solution.

To fully close the system of equations, compatibility relations are required. Based on physical observations, a common representation of these relations is given as follows[33]:

$$\begin{cases} h_f \geq 0 \\ \dot{m}_{ice} \geq 0 \\ h_f T_f \geq 0 \\ \dot{m}_{ice} T_f \leq 0 \end{cases} \quad (2.31)$$

CHAPTER III

3. CLEAN CASE STUDY

In this chapter, the aerodynamic performance of the NACA 0012 airfoil under clean (ice-free) conditions is investigated through Computational Fluid Dynamics (CFD) simulations. The clean case serves as the baseline reference for assessing the aerodynamic degradation caused by ice accretion in subsequent sections. All clean case simulations were conducted using ANSYS Fluent, a widely used CFD solver known for its robustness in external aerodynamics applications. To ensure reliable and accurate results, special attention was paid to the precise modeling of the airfoil geometry, the proper definition of the computational domain, and the generation of a high-quality structured mesh. These steps are critical to minimizing numerical errors and capturing flow features such as boundary layer development and potential flow separation, which are essential for accurately evaluating the lift, drag, and pressure distributions of the clean airfoil. The validated clean case results form the foundation upon which the aerodynamic consequences of different ice shapes and accretion scenarios will be systematically analyzed.

3.1 NACA 0012 GEOMETRY

Since there are numerous experimental and numerical studies available in the literature for the NACA 0012 airfoil, it was selected for validation purposes in both clean and icing cases. Additionally, due to the simplicity of its geometry, the NACA 0012 airfoil was used for investigating the effects of icing on aerodynamic performance.

The NACA 0012 airfoil has specific characteristics. The first two digits, 00, define the airfoil as symmetric, while the last two digits, 12, indicate that the maximum thickness of the airfoil is 12% of the chord length.

The geometry of the NACA 0012 airfoil used in the calculations was generated by connecting points on the coordinate plane. The general formula required to create the NACA 0012 geometry is given in the Equation 3.1.

$$y_t(x) = 5t\left(0.2969\sqrt{x} - 0.1260x - 0.3516x^2 + 0.2843x^3 - 0.1015x^4\right) \quad (3.1)$$

In this equation, $y_t(x)$ represents the airfoil thickness at a given position x, where t denotes the maximum thickness of the airfoil. The variable x corresponds to the position along the chord from the leading edge to the trailing edge. The geometric profile of the NACA 0012 airfoil used in this study is illustrated in Figure 3.1.

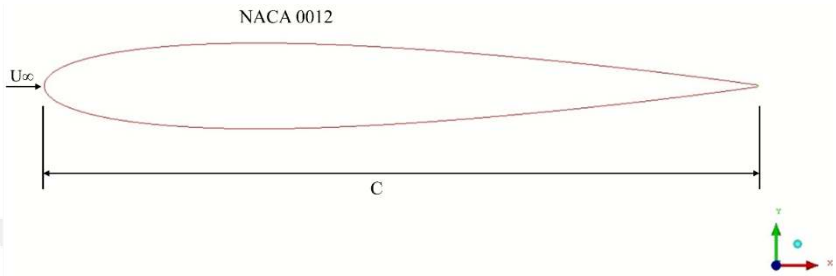

Figure 3.1: NACA 0012 Airfoil

3.2 COMPUTATIONAL DOMAIN

The computational domain and mesh structure to be used in the simulations were prepared using the ANSYS ICEM-CFD. A C-type mesh domain was chosen due to its suitability for airfoil simulations. The boundary conditions were defined as a velocity inlet at the front and a pressure outlet at the back of the domain. The NACA 0012 airfoil was defined as a no-slip wall boundary condition. It was placed 10 chords away from the inlet and 30 chords away from the outlet. A schematic representation of the computational domain and the defined boundary conditions is provided in Figure 3.2.

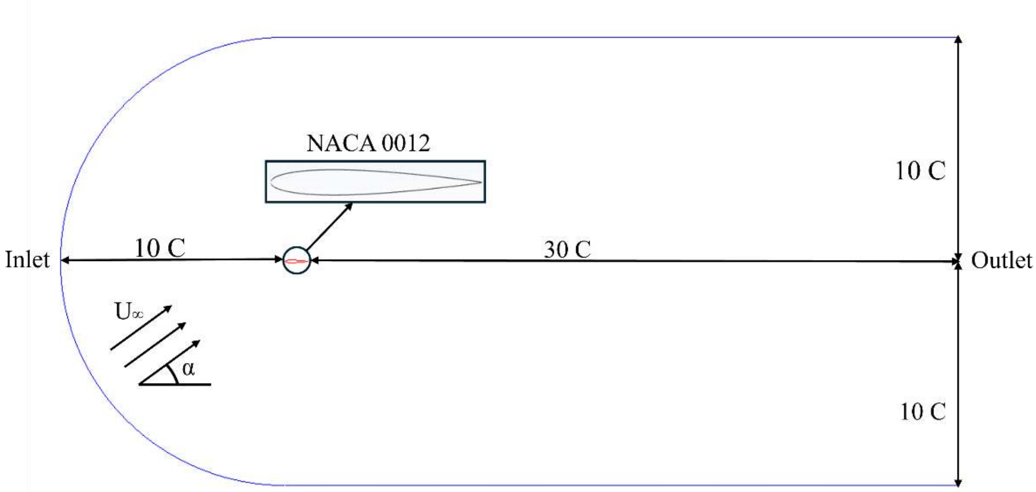

Figure 3.2: C-Type Computational Domain

3.3 MESH INDEPENDENCY STUDY

Mesh independency study is a critical step to ensure the accuracy and reliability of numerical simulations. The purpose of this study is to check whether the obtained simulation results stabilize as the mesh resolution increases. When mesh independency is achieved, the numerical solution no longer significantly changes with further mesh refinement, indicating minimized discretization errors. In this study, drag coefficient was selected as a control parameter to assess convergence behavior. In simulations conducted on the NACA 0012 airfoil at a 0° angle of attack and a Reynolds number of 6 million, the change in drag coefficient with increasing the number of elements is shown in Figure 3.3.

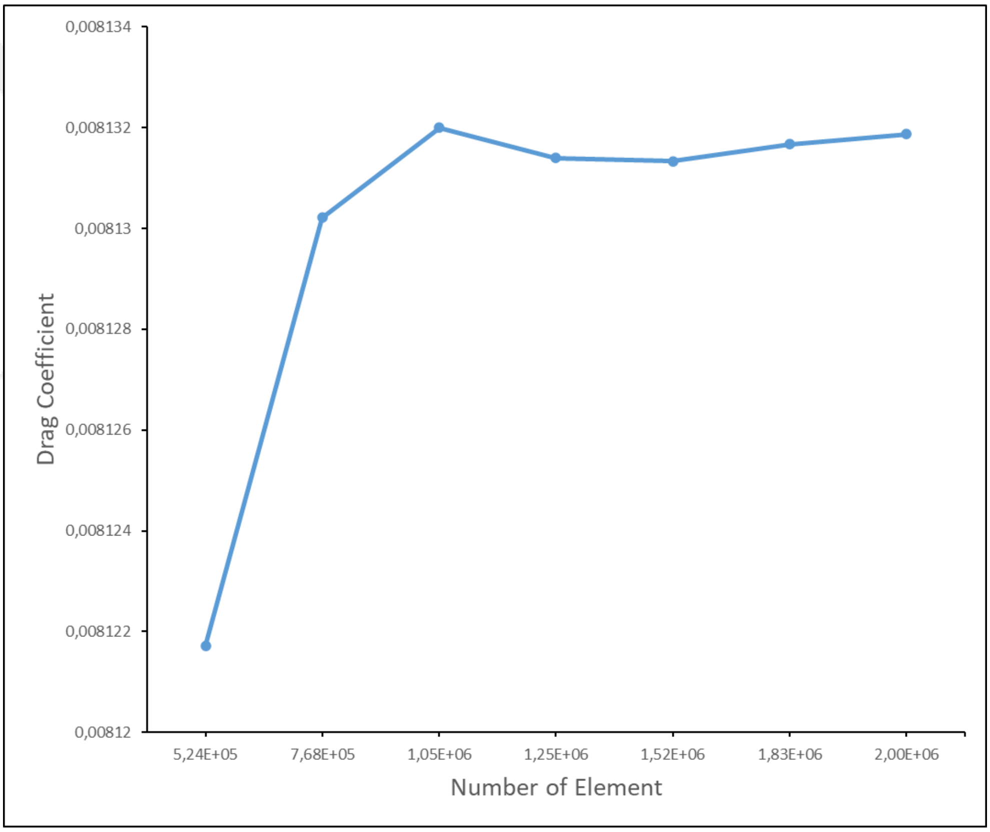

Figure 3.3: Variation of Drag Coefficient with different number of elements

As illustrated in the graph, increasing the number of mesh elements beyond approximately 1.5 million does not lead to a significant change in the drag coefficient. Therefore, it can be concluded that using around 1.5 million elements provides an optimal balance between accuracy and computational efficiency, as further refinement only results in unnecessary increases in computation time.

3.4 MESH SENSITIVITY ANALYSIS

Mesh quality is a critical factor influencing the accuracy of CFD simulations. In particular, employing a high-resolution mesh in the leading and trailing edge regions of the airfoil is essential for capturing the detailed flow characteristics accurately. This level of refinement is especially important for both clean and iced configurations, where subtle geometric and flow variations can significantly affect the aerodynamic performance. The overall mesh structure of the computational domain and close-up views around the NACA 0012 airfoil are presented in Figures 3.4 and 3.5, respectively.

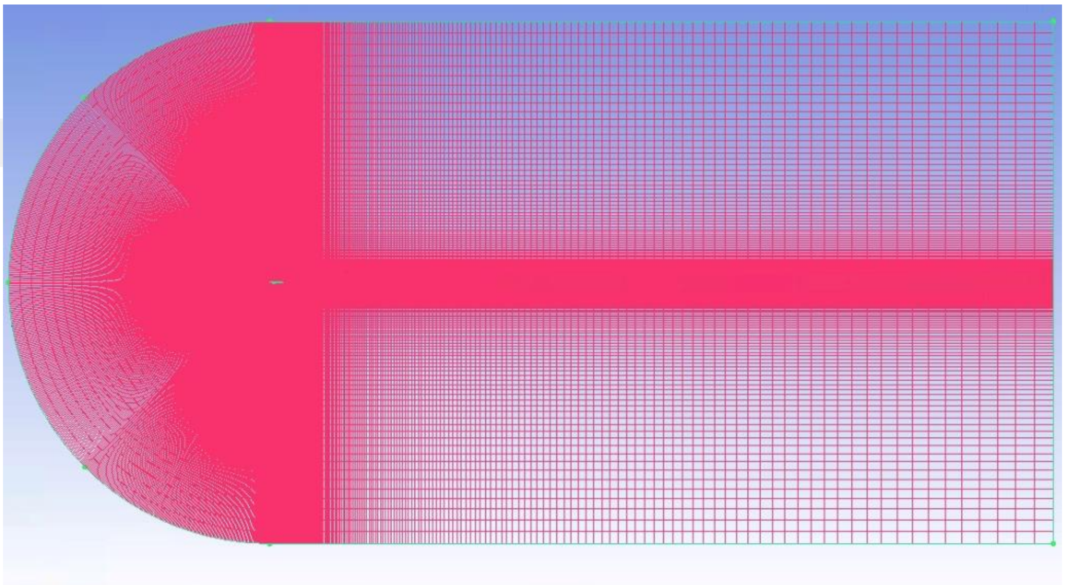

Figure 3.4: Mesh structure of the full computational domain

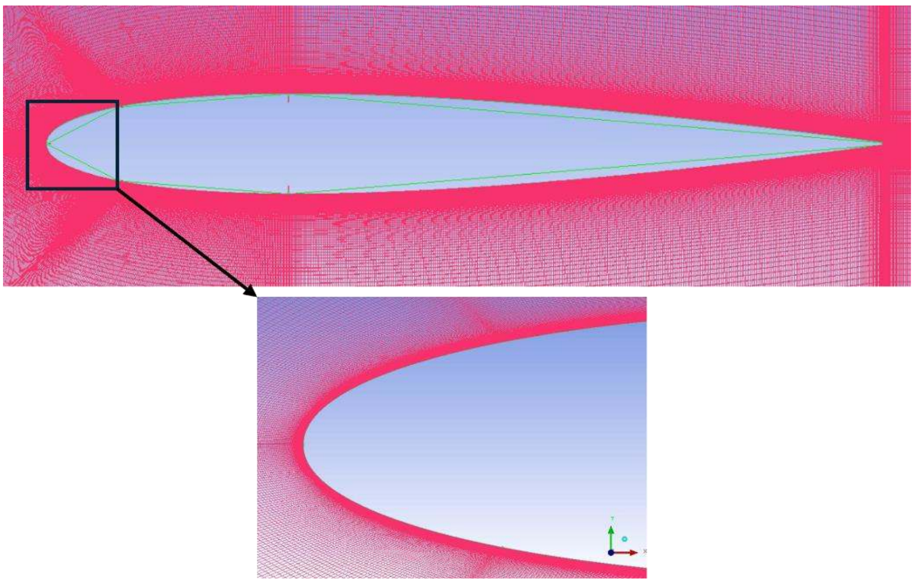

Figure 3.5: Close-up views of the mesh around the NACA0012 airfoil

In order to evaluate the mesh quality, general and orthogonal mesh quality values were taken into account.

General mesh quality values are shown below. In general, values closer to 1 indicate higher mesh quality. As can be seen in Table 3.1, more than 97% of the elements have values between 0.9 and 1.

Table 3.1: General Quality Values

Quality Values	Percentage of Elements (%)
0.95-1	96.8%
0.9-0.95	1.03%

Similarly, values close to 1 in orthogonal mesh quality indicate that the cell quality is good. As can be seen in Table 3.2 below, more than 92% of the elements have values between 0.9 and 1.

Table 3.2: Orthogonal Quality Values

Orthogonal Quality Values	Percentage of Elements (%)
0.95-1	88.7%
0.9-0.95	3.59%

3.5 Y+ VALUE

The y+ value is a dimensionless parameter used in computational fluid dynamics analyses, especially when determining the initial cell height in the boundary layer. It is very important to choose the y value correctly because it significantly affects the accuracy of the analyses. Y+ value is defined in Equation 3.2 below.

$$y^{+} = \frac{y \times u_{\tau}}{\nu} \tag{3.2}$$

In the equation, y is the distance from the wall to the center of the first mesh cell (m). u_{τ} is the friction velocity (m/s), which depends on the wall shear stress and ν is the kinematic viscosity (m^2/s).

In this study, the y+ value was taken as 1 and the first cell height was calculated as 6 x 10^{-6}.

3.6 CLEAN CASE VALIDATION

After determining a suitable geometry and mesh structure, a detailed validation study was conducted on the clean NACA 0012 airfoil to verify the accuracy and reliability of the CFD simulations. It is particularly important to accurately predict the lift and drag coefficients, as they are key indicators of how icing affects the aerodynamic performance of the airfoil.

In the validation studies, the aerodynamic performance of the NACA 0012 airfoil at different angles of attack (0°, 4°, 8°, 12°, 16°) was investigated with a chord length of 1 m and a Reynolds number of 6 x 10^6. Three turbulence models that are widely used in the literature were compared in the analyses. These turbulence models are the k-ω model, the Transition SST model and the Spalart–Allmaras model. The obtained lift coefficient and drag coefficient values were compared with NASA Ladson's experimental results [35].

As shown in Figure 3.6, the lift coefficients predicted by all three turbulence models exhibit good agreement with the experimental data across the entire range of angles of attack. This consistency indicates the reliability of the numerical setup in capturing the aerodynamic behavior of the airfoil under clean conditions.

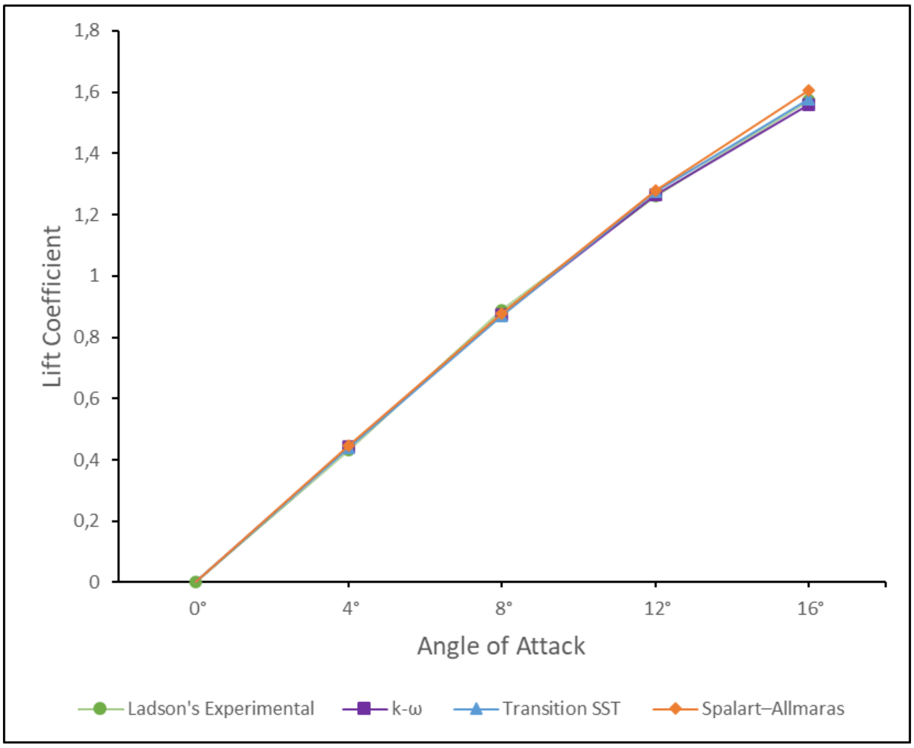

Figure 3.6: Variation of Lift Coefficient with different turbulence models

In the Figure 3.7, the obtained drag coefficients for the k-ω and Spalart–Allmaras models are in good agreement with the experimental data especially at angles of attack of 0°, 4°, and 8°.

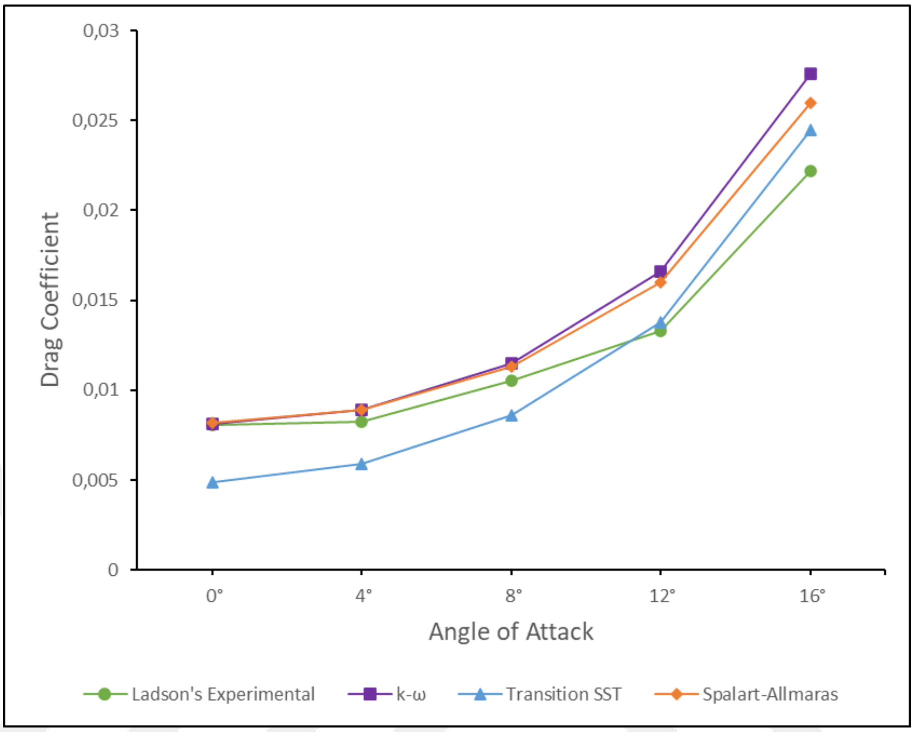

Figure 3.7: Variation of Drag Coefficient with different turbulence models

When comparing the turbulence models, it is observed that the lift coefficient is predicted with less than 2% error across all models. However, as the angle of attack increases, deviations between the numerical and experimental results become more pronounced for each model. On the other hand, differences between the models are more evident in the drag coefficient predictions. In terms of overall accuracy, the Spalart–Allmaras model demonstrated superior performance, achieving the lowest average error at approximately 6%, making it the most accurate among the evaluated models.

3.7 CLEAN RESULTS

As the final step of the clean case studies, clean case analyses were performed at a chord length of 0.53 m and a Reynolds number of 2.5 million, representing the conditions under which the icing simulations were performed. The analyses were performed at angles of attack of 2°, 4°, 6°, 8°, 10°, and 12° with using Spalart-

Allmaras turbulence model. The results of these analyses are presented in Figures 3.8 as a reference for future icing simulations.

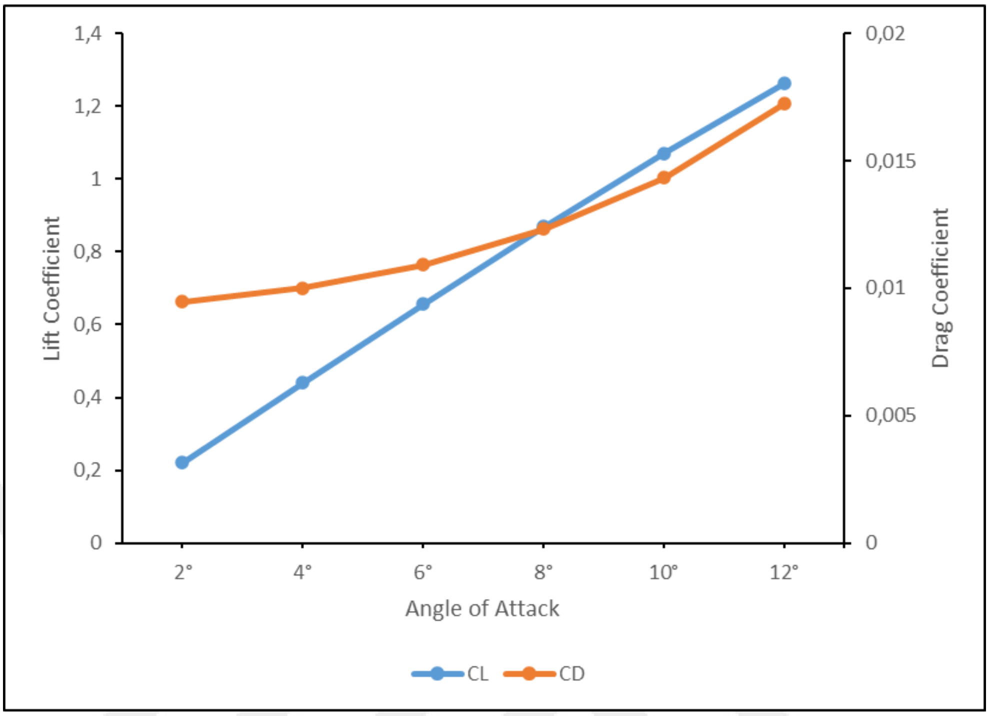

Figure 3.8: Clean case result

CHAPTER IV

4. ICED CASE STUDY

In the present icing simulations, the computational domain and mesh structure established for the clean configuration were utilized as a basis. Flow field solutions were carried out in the FENSAP module using the Spalart–Allmaras turbulence model. A no-slip wall boundary condition was imposed on the airfoil surface, with the wall temperature specified as the stagnation temperature plus 10 K. Droplet trajectory calculations were performed in the DROP3D module, assuming a monodisperse droplet distribution. Subsequently, the ICE3D module was employed to simulate ice accretion on the airfoil surface. More detailed technical descriptions of these modules and their implementations are provided in the methodology section of this thesis.

4.1 MULTI-SHOT ICE ACCRETION

Multi-shot approach is a method used to more realistically model the growth processes of the ice on the airfoil surface over time. In this approach, ice accretion is simulated sequentially by dividing it into specific time steps. At each step, new ice accretion is calculated and the existing ice geometry is updated. FENSAP-ICE software can perform icing analysis using both single-shot and multi-shot approaches.

Wright [36] emphasized that one of the most important factors for accurate ice shape prediction is the use of multiple time steps, and stated that within each individual time step, the maximum allowable ice thickness should be limited to no more than 1% of the airfoil's chord length. To determine the total number of time steps, the following empirical correlation was used:

$$n = \frac{LWC \times V \times Time}{Chord\ Length \times \rho_{ice} \times 0.01} \tag{4.1}$$

In the equation, n represents the number of time steps, V is the velocity and ρ_{ice} is the ice density. The term (LWC)(V)(t)/(ρ_{ice}) represents the maximum amount of ice that could accumulate on the impact surface during the exposure time.

According to this empirical formulation, five time steps would be sufficient under the current operating conditions. Nevertheless, six time steps were selected to slightly enhance the accuracy of the simulation. Figure 4.1 presents an example analysis of the ice accretion process, divided into six time steps of 60 seconds each, for a total simulation duration of 360 seconds. The curves, color-coded from 1 to 6, illustrate the evolution of the airfoil shape as a function of time. As observed, ice accretion initially begins at the leading edge and gradually extends both upward and downward. The ice growth eventually forms a structure resembling "horn ice," characterized by an upward-curving accumulation near the leading edge.

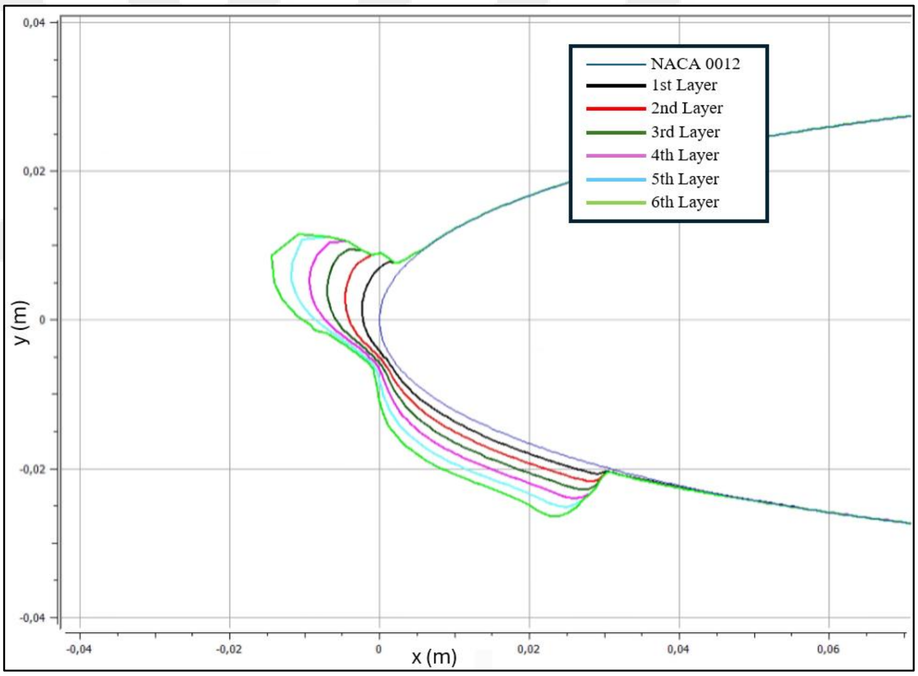

Figure 4.1: Ice accretion development over six steps in the multi-shot simulation

4.2 ICED CASE VALIDATION

In order to validate the accuracy and reliability of the CFD simulations under icing conditions, a specific ice accretion case was selected from the experimental study conducted by Shin and Bond [16], which was supported by NASA. The tests were conducted in the NASA Lewis Icing Research Tunnel, which has a test section measuring 6 ft. high, 9 ft. wide, and 20 ft. long. A NACA 0012 airfoil with a span of 6 ft. and a chord length of 21 in. was used as the test model. Throughout all experiments, the angle of attack was kept constant at 4°. In this validation study, the primary objective was to evaluate how closely the simulation results matched with the experimentally obtained ice shape and drag coefficient under specific test conditions. The experimental test parameters used for validation are summarized in Table 4.1.

Table 4.1: Experimental conditions for iced case validation study

AoA [°]	Temperature [° C]	Velocity [m/s]	LWC [g/m^3]	MVD [μm]	Exposure Time [s]
4	-5.5	67.056	1	20	360

The ice shape comparison presented in Figure 4.2 shows a high level of agreement between ice shape obtained from this study and the experimental ice shape geometry. The ice accretion predicted by this study closely follows the contour of the reference ice shape. The upper and lower limits of the accreted ice predicted by the current model show good agreement with the experimental data. When the error is calculated in terms of maximum ice thickness, the numerical prediction gives the location of maximum thickness at approximately x/c = 0.028, while the experimental data indicates it at approximately x/c = 0.0256. This corresponds to a 9.5% deviation in the prediction of the maximum ice thickness location. However, such behavior is also consistent with findings reported in the literature. For example, in the study by Liu et al. [37], the maximum ice thickness near the stagnation point was predicted greater in numerical simulations than in experiments.

Upon examination of the current airfoil, it is observed that the liquid droplets do not freeze immediately upon impact with the surface. Instead, influenced by the incoming airflow, a water film forms and moves upward along the surface, gradually freezing over time. This process leads to the formation of an upward-curving ice protrusion near the leading edge of the airfoil, exhibiting characteristics of ice accretion. The resulting ice shape is irregular, with the maximum ice thickness typically occurring around the stagnation point. This phenomenon significantly affects the geometry of ice accretion on the aerodynamic surface and may lead to notable performance degradation.

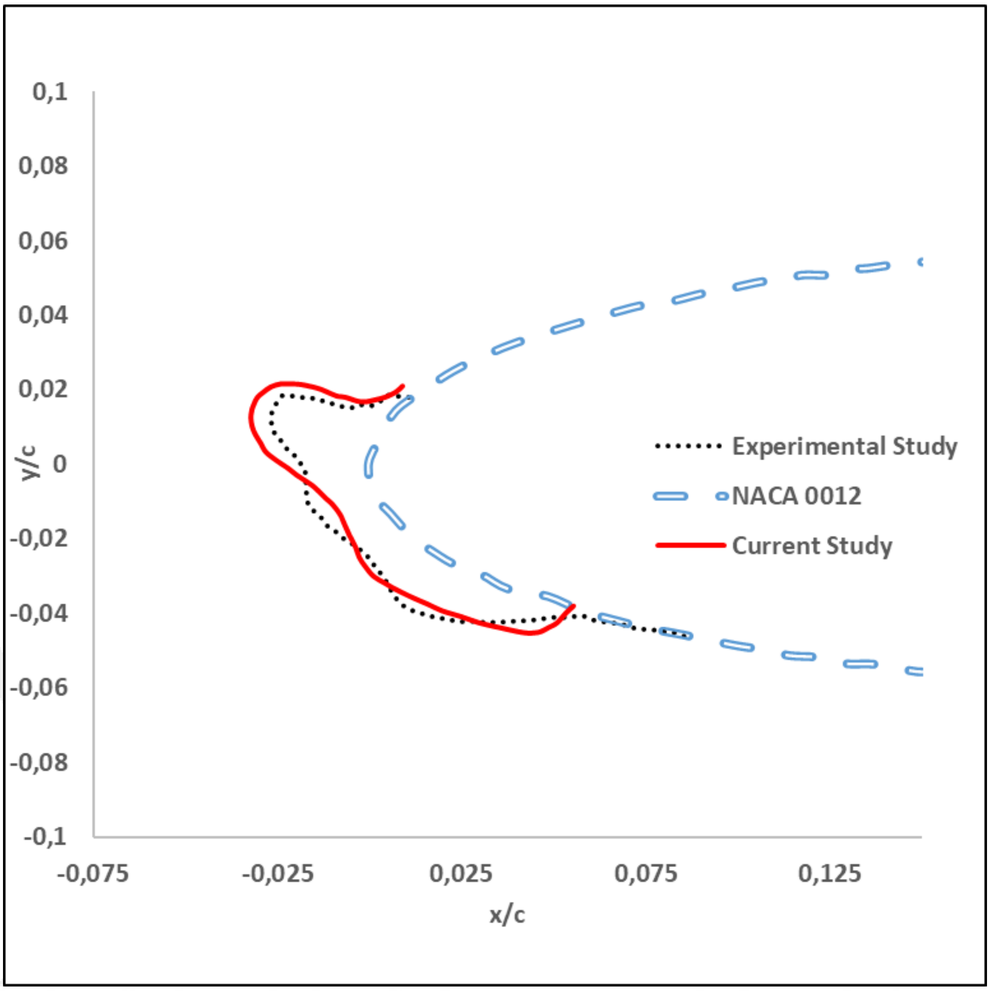

Figure 4.2: Comparison of ice shapes for validation study

According to the calculation based on the definition provided by Wright [36], the maximum ice thickness at the end of the 6 steps corresponds to approximately 3% of the chord length, which remains below the recommended threshold of 1% at an any single step.

As the second step of the icing validation study, the drag coefficient obtained from the numerical simulation was compared with the experimental data. The experimentally reported drag coefficient for the iced NACA 0012 airfoil is 0.03152 under the icing conditions specified in Table 4.1, while the simulation yielded a drag coefficient of 0.02648. This corresponds to a relative error of approximately 16%, indicating that the numerical model slightly underpredicts the drag caused by ice accretion. The discrepancy may arise from simplifications in the ice roughness modeling, mesh resolution, or turbulence modeling assumptions.

Table 4.2: Iced case validation study results

Parameter	Experimental Value	Numerical Value	Relative Error (%)
CD	0.03152	0.02648	16

The validation results show that the numerical simulation accurately captures both the ice shape and its aerodynamic effects. Although some minor differences exist between the simulated and experimental data, CFD-based method developed in this study has proven capable of accurately solving the icing problem. This validated setup makes it possible to conduct detailed parametric studies under varying icing conditions, allowing for the analysis of their effects on both ice shape formation and aerodynamic performance.

CHAPTER V

5. RESULTS

This chapter presents comprehensive findings on ice accretion of the NACA 0012 airfoil under different atmospheric and operational conditions. The influence of fundamental parameters such as liquid water content (LWC), median volume diameter (MVD), airspeed, exposure time and angle of attack on ice shape, aerodynamic performance (lift and drag coefficients), ice thickness distribution, and droplet collection efficiency is systematically investigated.

5.1 EFFECT OF ANGLE OF ATTACK ON ICING

The effect of angle of attack on ice accretion was investigated at angles of 2°, 4°, 6°, 8°, 10°, and 12°. The detailed parameters used in these simulations are summarized in the table below.

Table 5.1: Icing conditions for different angles of attack

Simulation Cases	SC1	SC2	SC3	SC4	SC5	SC6
AoA [°]	**2**	**4**	**6**	**8**	**10**	**12**
Temperature [° C]	-5.5	-5.5	-5.5	-5.5	-5.5	-5.5
Velocity [m/s]	67.056	67.056	67.056	67.056	67.056	67.056
LWC [g/m^3]	1	1	1	1	1	1
MVD [µm]	20	20	20	20	20	20
Exposure Time [s]	360	360	360	360	360	360

5.1.1 Effect of Angle of Attack on Ice Shape and Ice Thickness

Figure 5.1 depicts the effect of different angles of attack (AoA) on ice accretion. As the AoA changes, it is evident that the ice horns vary in both position and height, with the symmetry of the ice accretion pattern being altered. With increasing AoA, the upper-surface horn tends to grow closer to the symmetry point on the airfoil, which promotes earlier flow separation. Concurrently, the ice thickness on the lower surface decreases, while that on the upper surface increases noticeably. This shift in the ice accretion pattern becomes particularly prominent at an AoA of 12°, where the upper surface horn exhibits significant growth and the ice formation extends along the x-axis to approximately 0.08 m.

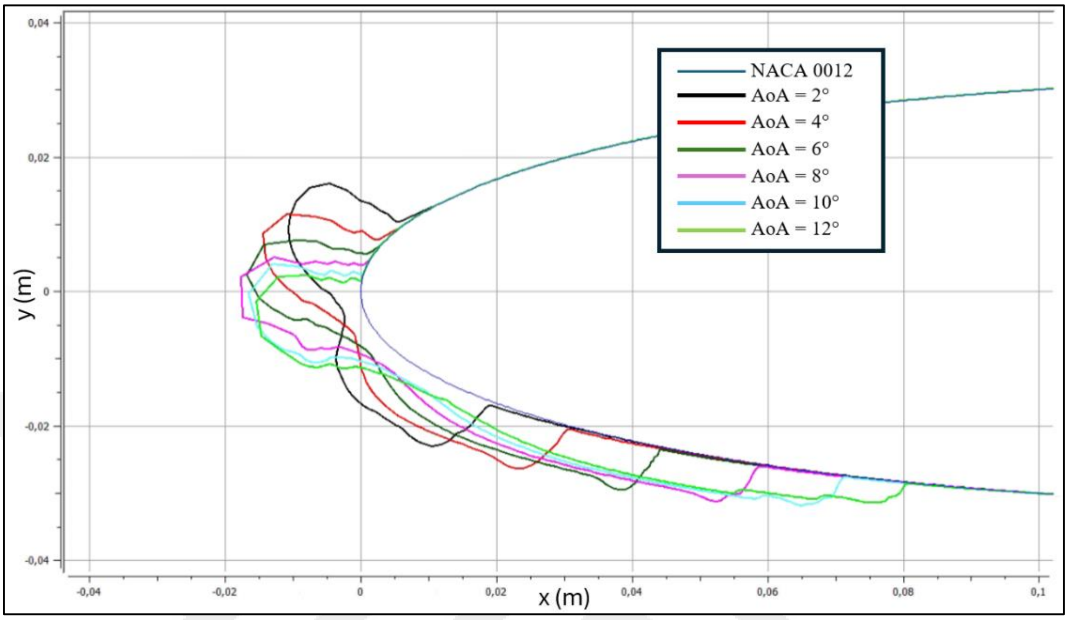

Figure 5.1: The effect of angle of attack on ice shape

Figure 5.2 presents the variation of ice thickness distribution over the airfoil surface for different angles of attack. At lower AoA values (2° and 4°), the maximum ice thickness is observed on the upper surface near the leading edge, and the profile retains a largely symmetric form. As the AoA increases, the peak ice thickness progressively shifts toward the lower surface, and the initially symmetric profile becomes increasingly asymmetric. This change is accompanied by a reduction in ice accumulation on the upper surface and a marked increase on the lower surface, particularly evident at higher AoA values. The maximum ice thickness is recorded at AoA = 8°, reaching approximately 0.018 m. The development of asymmetry in the ice thickness profile is of particular concern, as it disrupts the aerodynamic balance of the airfoil, alters the pressure distribution, and promotes earlier flow separation, leading to greater performance degradation. These observations are consistent with the findings of Lu et al. [25], who reported a similar transition from symmetric to asymmetric ice accretion patterns with increasing AoA.

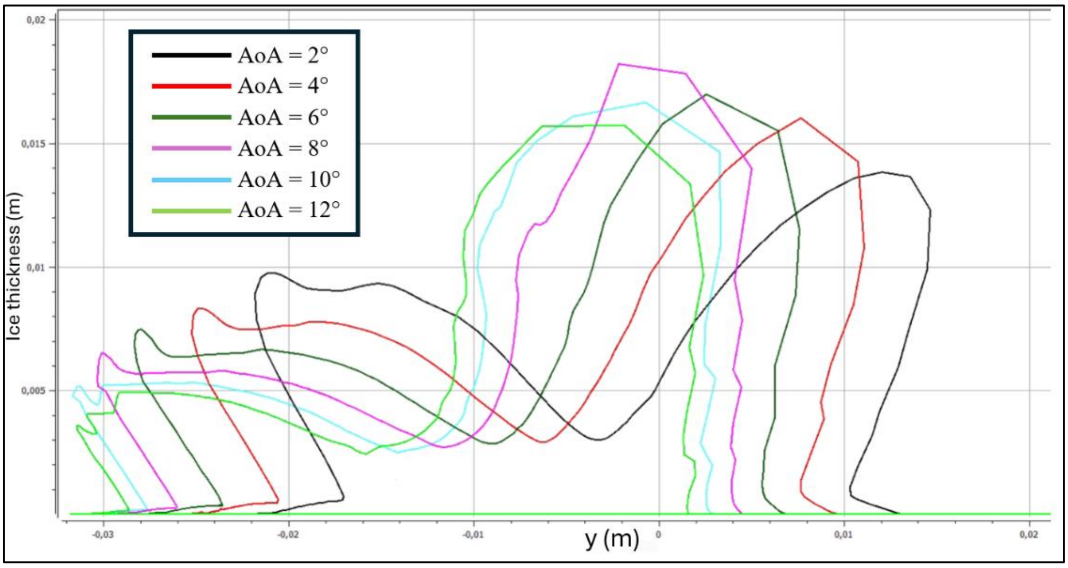

Figure 5.2: The effect of angle of attack on ice thickness

5.1.2 Effect of Angle of Attack on Droplet Collection Efficiency

Figure 5.3 presents the influence of varying the angle of attack on the collection efficiency. The overall trend indicates that, with an increase in the angle of attack, the distribution of droplets gradually shifts toward the lower surface of the airfoil. Notably, at AoA = 12°, nearly all droplets are captured by the lower surface of the airfoil.

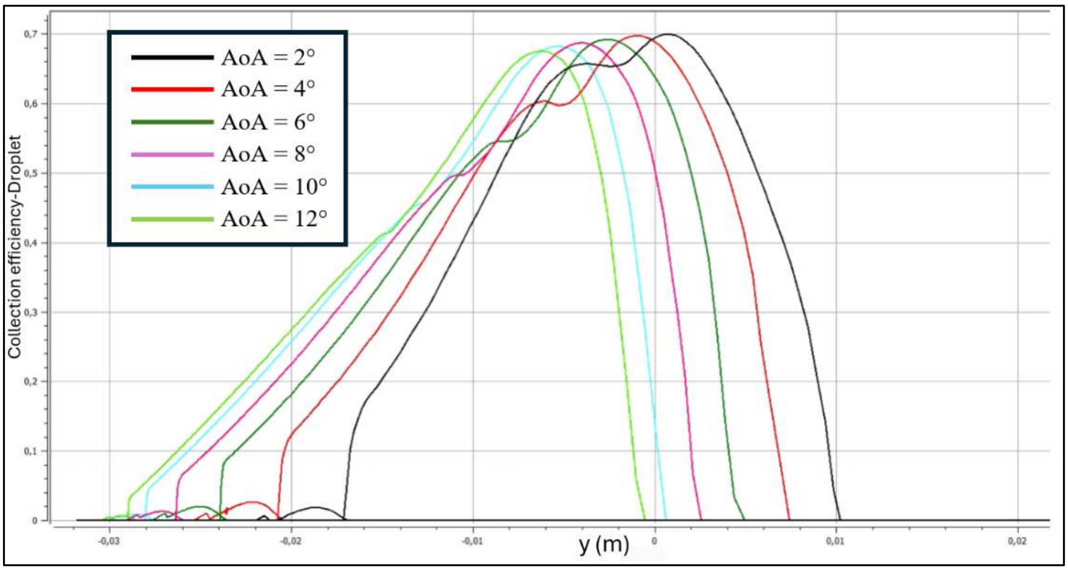

Figure 5.3: The effect of angle of attack on collection efficiency

5.1.3 Effect of Angle of Attack on Performance Degradation

Figures 5.4 and 5.5 compare the lift and drag coefficients of clean and iced airfoils across a range of angles of attack. It is observed that an increase in the angle of attack leads to a significant rise in drag and a decrease in lift. Furthermore, the earlier onset of stall is clearly evident from the variation in the lift coefficient. The maximum lift coefficient of the iced airfoil is reduced by approximately 56% compared to the clean configuration, and stall occurs around at AoA = 10°, whereas the clean airfoil sustains lift up to 12° without a sharp drop. Similarly, the effect of icing on the drag coefficient is significant at every angle of attack. Starting from 8°, a dramatic rise in drag coefficient is observed. At AoA = 12°, the drag coefficient of the iced airfoil increases by approximately 625% compared to the clean airfoil.

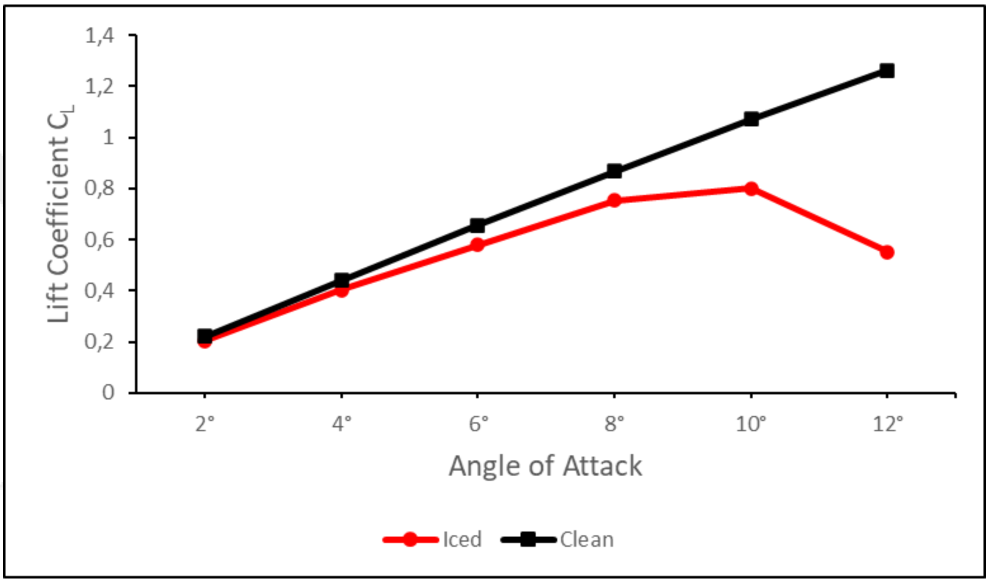

Figure 5.4: The effect of angle of attack on lift coefficient

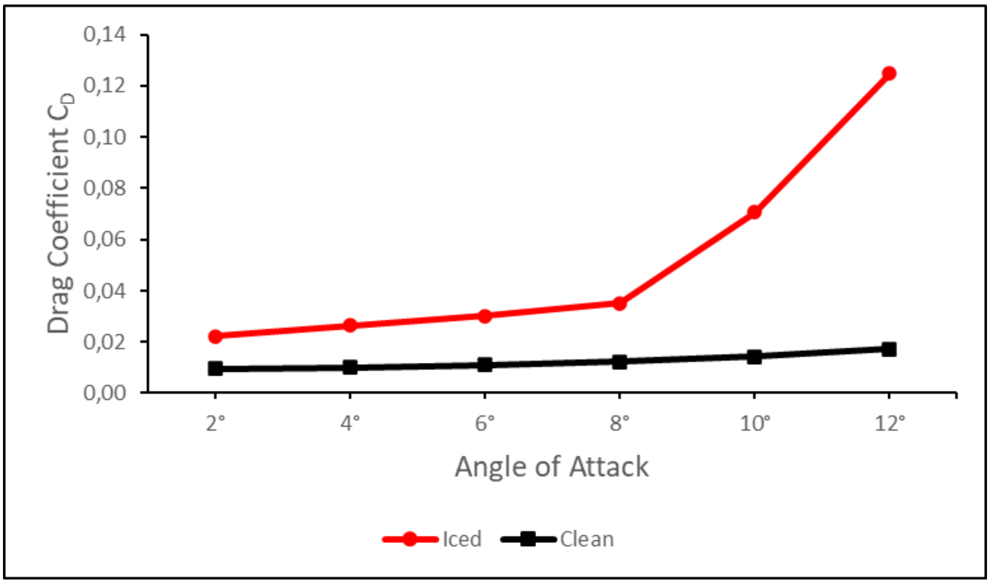

Figure 5.5: The effect of angle of attack on drag coefficient

5.1.4 Contour Investigation of Turbulent Viscosity at Different AoA

Figure 5.6 presents the turbulent viscosity contours for clean and iced cases at different angles of attack. These contours illustrate the influence of turbulence on momentum transfer within the flow. Regions with high turbulent viscosity indicate intense turbulence, flow separation, and vortex formation, whereas areas with low turbulent viscosity represent attached, orderly flow. Examination of the clean airfoil reveals that the flow remains well-attached to the surface with no evident separation. At AoA = 10°, a thin turbulent region emerges, indicating the onset of flow separation. In contrast, for the iced airfoil, turbulence formation is already observed immediately downstream of the ice shape even at AoA = 2°. The increased surface roughness accelerates the breakdown of the boundary layer. As the AoA increases, the rough ice accretion near the leading edge further disturbs the flow, causing a progressive rise in turbulent viscosity, and the separation region extends toward the leading edge. At the highest examined AoA of 12°, the separation reaches nearly to the stagnation point. This phenomenon is consistent with the sharp drop in lift coefficient and the substantial increase in drag, providing a visual explanation of the observed aerodynamic performance degradation.

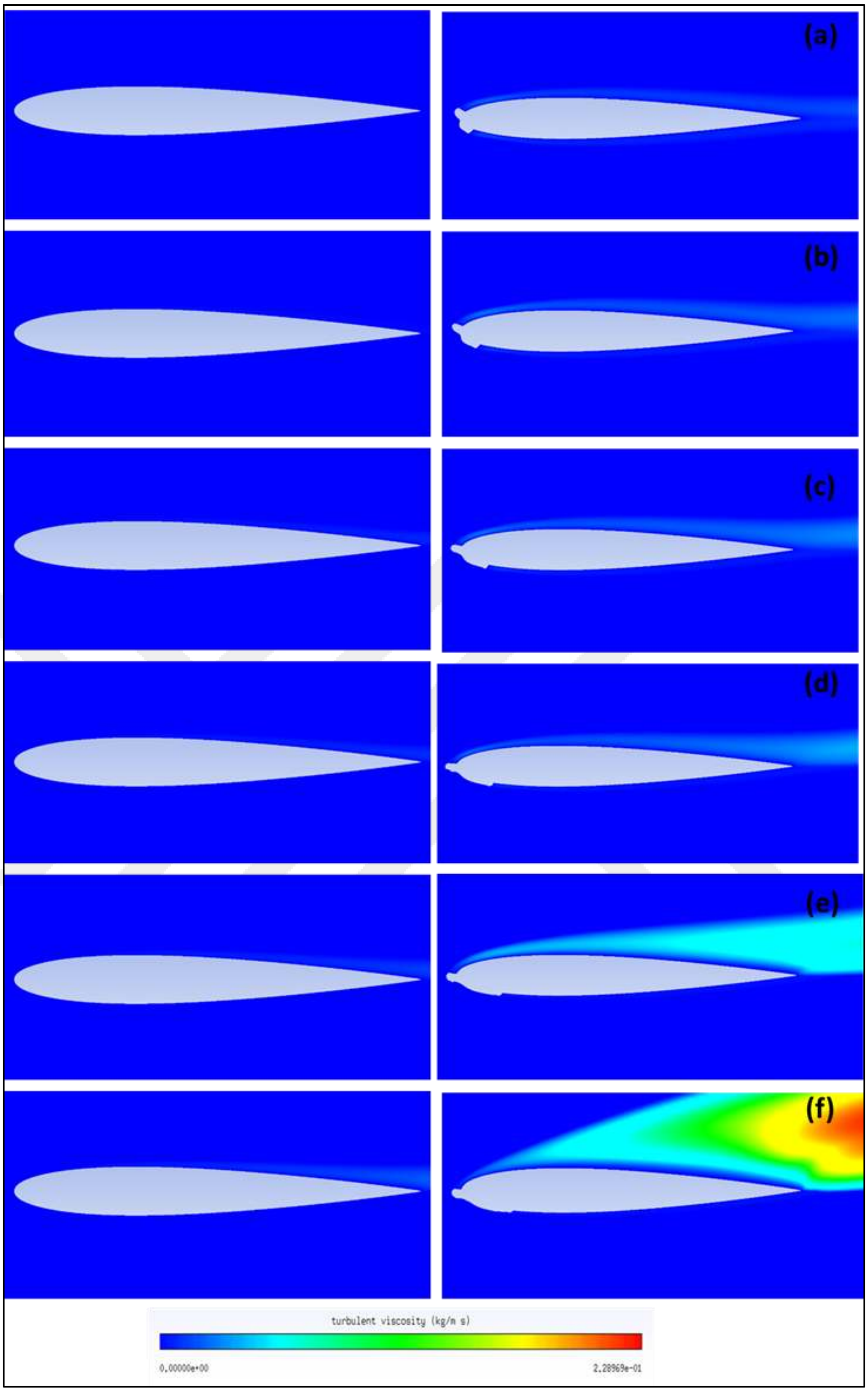

Figure 5.6: Turbulent viscosity contours for AoA (a) 2°(b) 4° (c) 6° (d) 8° (e) 10° (f) 12°

5.2 EFFECT OF LWC ON ICING

In this section, liquid water content values of 0.75 g/m^3, 1.0 g/m^3, 1.25 g/m^3, 1.5 g/m^3 and 1.75 g/m^3 were selected to investigate their effects on ice accretion, and the specific icing conditions are presented in the table below.

Table 5.2: Icing conditions for different LWC values

Simulation Cases	SC7	SC8	SC9	SC10	SC11
AoA [°]	4	4	4	4	4
Temperature [° C]	-5.5	-5.5	-5.5	-5.5	-5.5
Velocity [m/s]	67.056	67.056	67.056	67.056	67.056
LWC [g/m^3]	**0.75**	**1**	**1.25**	**1.5**	**1.75**
MVD [μm]	20	20	20	20	20
Exposure Time [s]	360	360	360	360	360

5.2.1 Effect of LWC on Ice Shape and Ice Thickness

Figure 5.7 illustrates the effect of varying liquid water content (LWC) on ice shape formation over the airfoil surface. As observed, the amount of ice accretion is minimal at LWC = 0.75 g/m^3. With increasing LWC, the overall ice mass increases. Furthermore, the ice features become more pronounced, with the lower-surface horn growing larger as the total ice mass increases. In particular, the horns near the leading edge become sharper and more protruding at higher LWC values. At the highest liquid water content of 1.75 g/m^3, the ice shape is the most irregular, and the area covered by ice on both the upper and lower surfaces of the airfoil reaches its maximum extent.

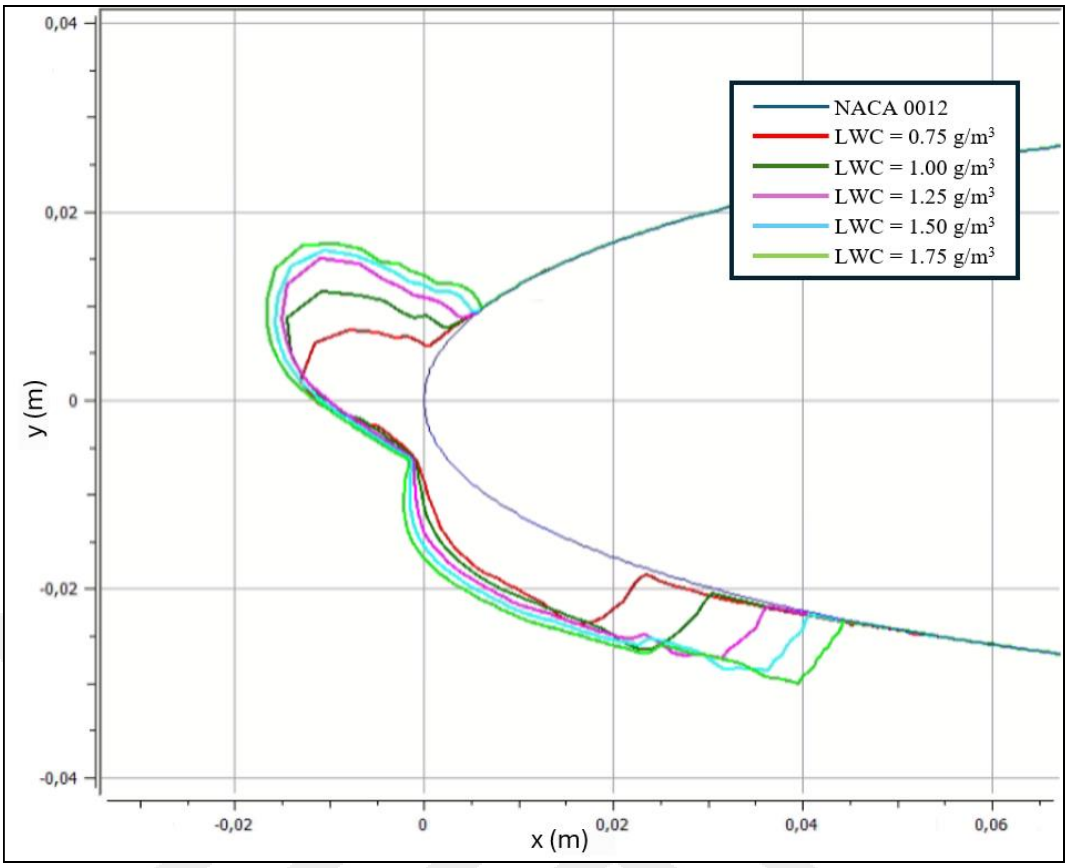

Figure 5.7: The effect of LWC on ice shape

Figure 5.8 illustrates the effect of varying liquid water content on the ice thickness. It can be observed from the graph that as the LWC increases, there is a significant rise in ice thickness, with the maximum ice thickness occurring on the upper surface of the airfoil.

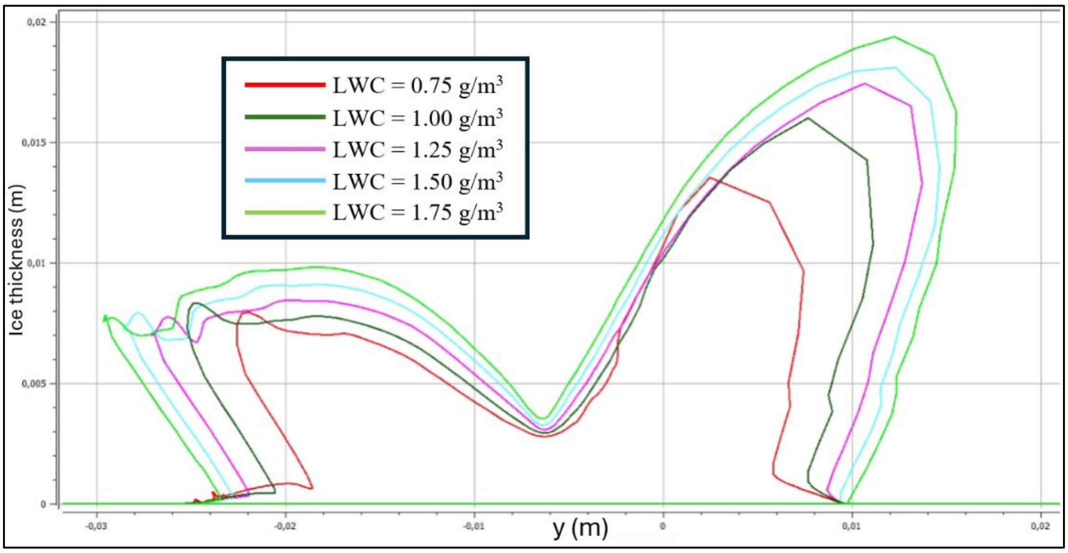

Figure 5.8: The effect of LWC on ice thickness

5.2.2 Effect of LWC on Droplet Collection Efficiency

Although the amount of ice accretion on the airfoil increases with higher LWC values, the influence of increasing LWC on the collection efficiency remains minimal. As shown in Figure 5.9, the distribution of collection efficiency under different LWC values is remarkably similar. An increase in droplet density or number does not alter the percentage of droplets impacting the surface; it only changes the total mass of water striking the surface. Nevertheless, it should be emphasized that even if the collection efficiency remains constant, a higher LWC increases the impinging mass flux, which in turn leads to thicker ice accretion and larger horn formations.

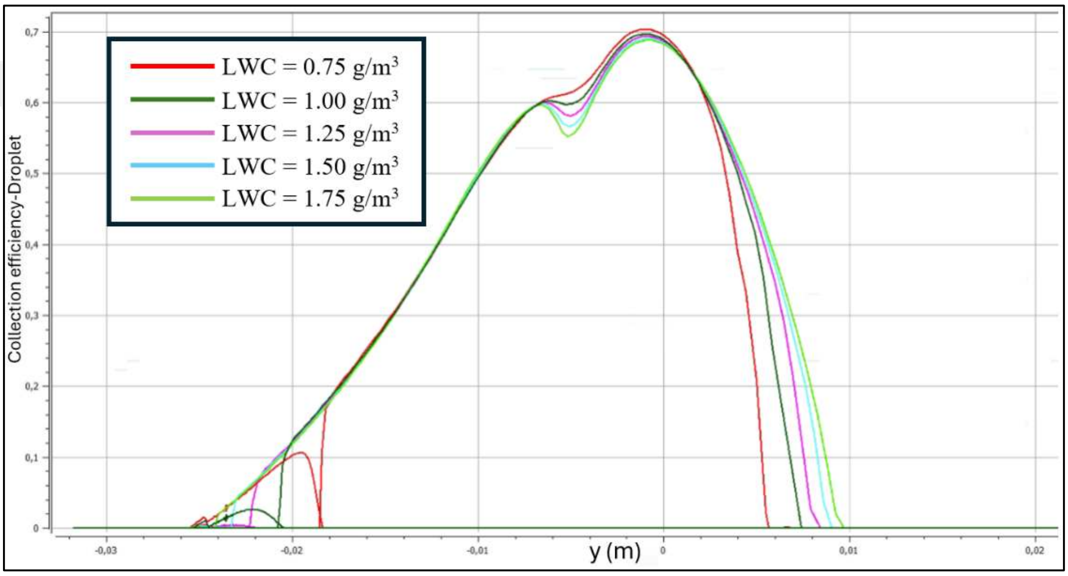

Figure 5.9: The effect of LWC on collection efficiency

5.2.3 Effect of LWC on Performance Degradation

Examination of Equation 2.17 reveals that an increase in LWC directly increases surface roughness. This mathematical relationship already indicates that LWC will have a dominant influence on drag force. Figure 5.10 and 5.11 present the effects of LWC on the lift and drag coefficients. With increasing LWC, a drastic rise in drag and a reduction in lift are observed. Moreover, the increase in drag is significantly more pronounced than the decrease in lift. This can be explained by the fact that lift is determined by the integral of the pressure difference, and the effects of local disturbances are partially distributed. In contrast, drag is directly affected by surface roughness and separation regions, as these disturbances increase momentum loss. Therefore, icing has a disproportionately large impact on Cd not only with respect to LWC but also for each individual parameter. At the highest examined LWC value of 1.75 g/m^3, the lift coefficient is reduced by up to 12%, whereas the drag coefficient increases by approximately 260%.

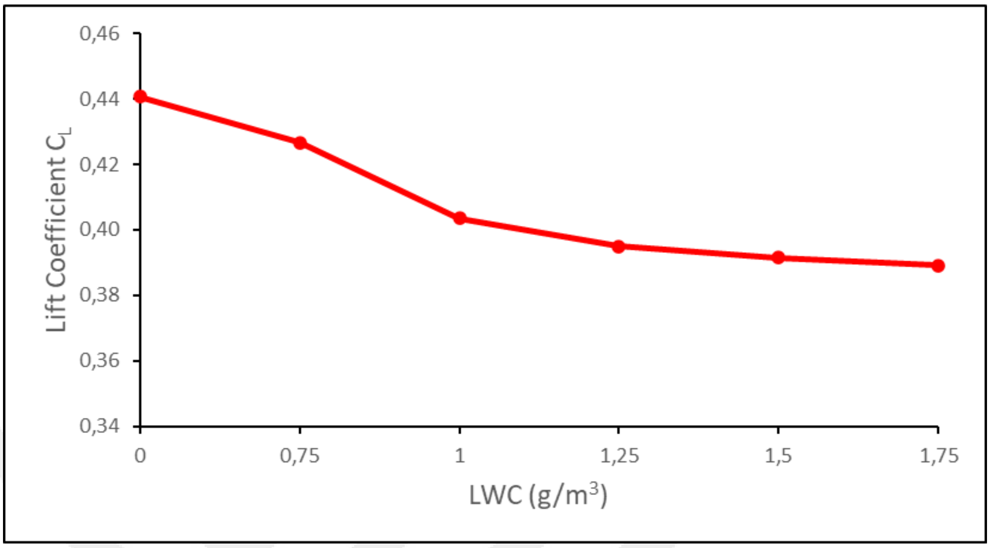

Figure 5.10: The effect of LWC on lift coefficient

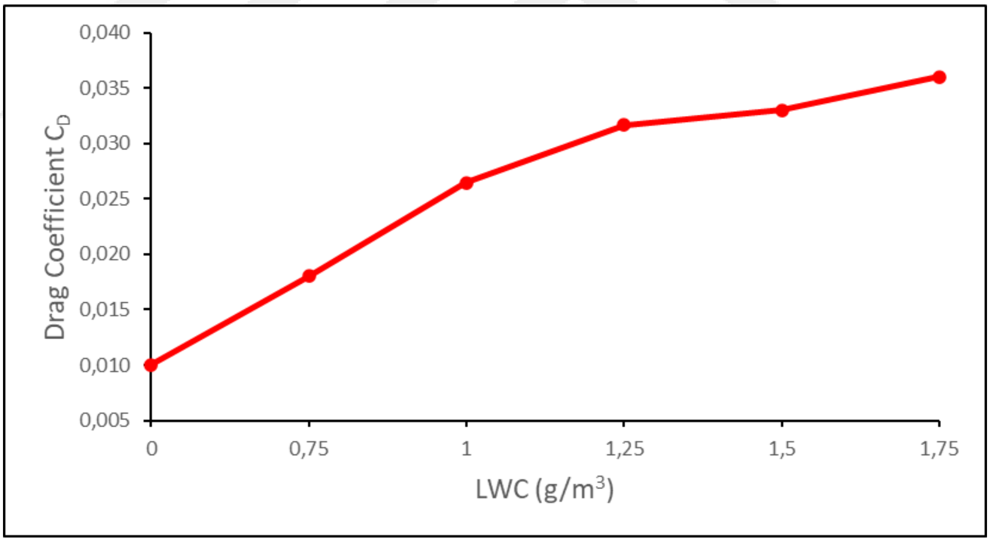

Figure 5.11: The effect of LWC on drag coefficient

5.2.4 Contour Investigation of Velocity at Different LWC

Figure 5.12 presents the velocity contours for different LWC values. As LWC increases, the ice horns formed at the leading edge alter the symmetric geometry of the airfoil, increasing both the camber and thickness. This increased curvature induces adverse pressure gradients, which, due to insufficient momentum within the boundary layer, lead to flow separation. With higher LWC, the adverse pressure gradient becomes more pronounced, and the separation point is pushed toward the leading edge. This forward shift becomes particularly evident for LWC values above 1.25 g/m^3.

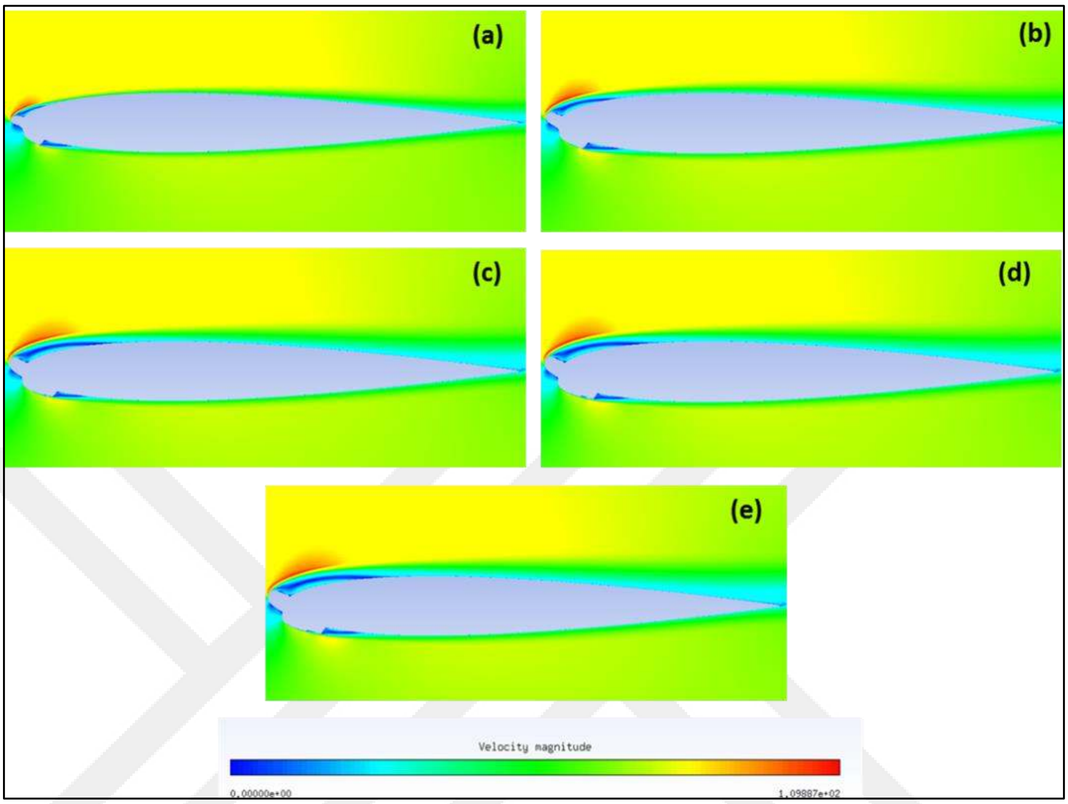

Figure 5.12: Velocity contours for LWC (a) 0.75 (b) 1 (c) 1.25 (d) 1.5 (e) 1.75 g/m^3

5.3 EFFECT OF MVD ON ICING

Median volumetric diameter (MVD) values of 10 µm, 20 µm, 30 µm, 40 µm, and 50 µm were chosen to analyze their influence on ice accretion. The detailed icing conditions are listed in the table below.

Table 5.3: Icing conditions for different MVD values

Simulation Cases	SC12	SC13	SC14	SC15	SC16
AoA [°]	4	4	4	4	4
Temperature [° C]	-5.5	-5.5	-5.5	-5.5	-5.5
Velocity [m/s]	67.056	67.056	67.056	67.056	67.056
LWC [g/m^3]	1	1	1	1	1
MVD [µm]	**10**	**20**	**30**	**40**	**50**
Exposure Time [s]	360	360	360	360	360

5.3.1 Effect of MVD on Ice Shape and Ice Thickness

The Stokes number is a dimensionless parameter that measures the ability of water droplets to adapt to changes in inertia while moving within a flow. As the MVD increases, the droplet diameter grows, resulting in a higher Stokes number. Figure 5.13 presents a comparison of ice shapes formed at various MVD values along the surface of the NACA 0012 airfoil. At lower MVD values (10 μm), corresponding to low Stokes numbers, ice accretion remains confined to a narrow region around the leading edge, forming relatively symmetric. As the MVD increases into the intermediate range (20–30 μm), the Stokes number approaches unity, leading to higher droplet collection efficiency. This results in more pronounced horn development on the upper surface and the initiation of horn formation on the lower surface. At higher MVD values (40–50 μm), the large droplet inertia promotes breakup and splashing upon impact, producing more irregular ice shapes. While horn heights remain substantial, the accretion spreads over a wider area along both surfaces. At an MVD of 50 μm, ice extends significantly along the lower surface, reaching approximately 0.15 m along the x-axis. This shows a clear increase in the total ice-covered area, even though the maximum horn height is slightly smaller.

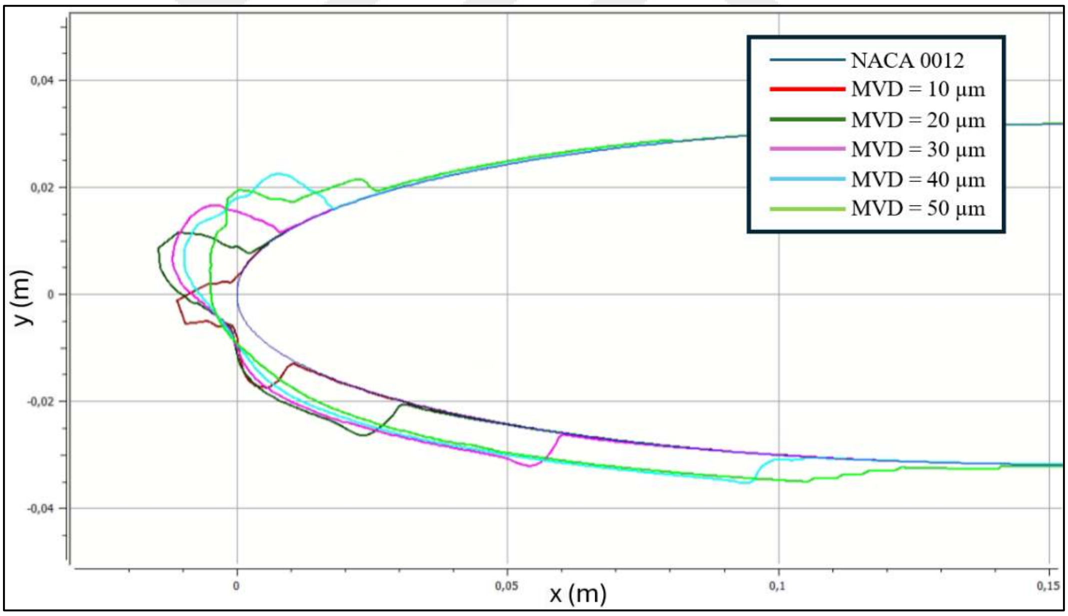

Figure 5.13: The effect of MVD on ice shape

Figure 5.14 demonstrates the distribution of ice thickness at different MVD values. Upon examining the graph, it is observed that the maximum ice thickness occurs at an MVD of 20 μm, reaching approximately 0.016 meters. Furthermore, as the MVD increases, ice accretion tends to spread over a more extensive area of the airfoil surface.

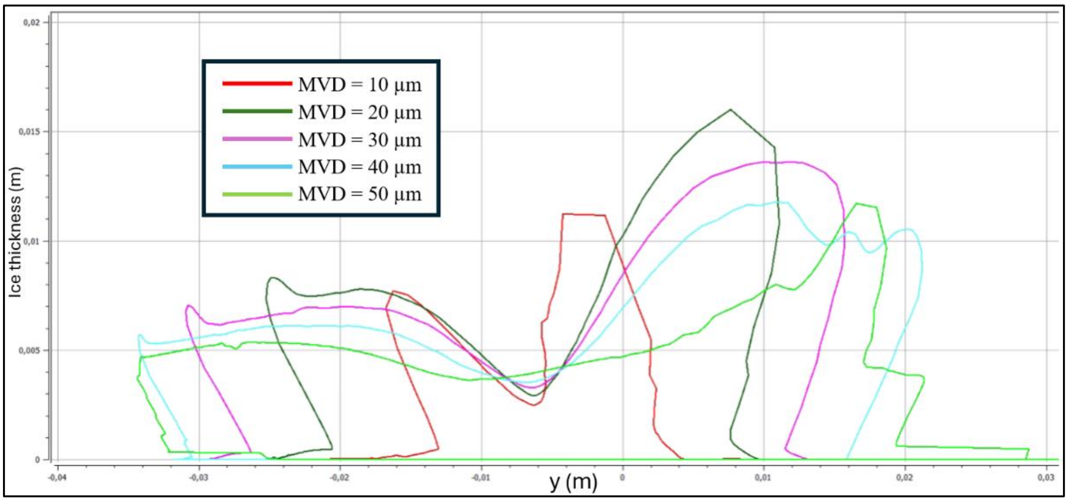

Figure 5.14: The effect of MVD on ice thickness

5.3.2 Effect of MVD on Droplet Collection Efficiency

The impact of increasing MVD values on droplet collection efficiency is presented in Figure 5.15. The results clearly indicate that MVD directly influences the collection efficiency distribution over the airfoil surface. When the MVD increases from 10 µm to 20 µm, the collection efficiency rises by approximately 40%; an increase from 20 µm to 30 µm results in a 15% increase; from 30 µm to 40 µm, the increase is about 7%; and from 40 µm to 50 µm, it is approximately 5%. A similar result was reported by Homola et al. [38], who stated that an increase in MVD enhances droplet collection efficiency, which in turn leads to an expansion of the ice-covered area on the airfoil surface.

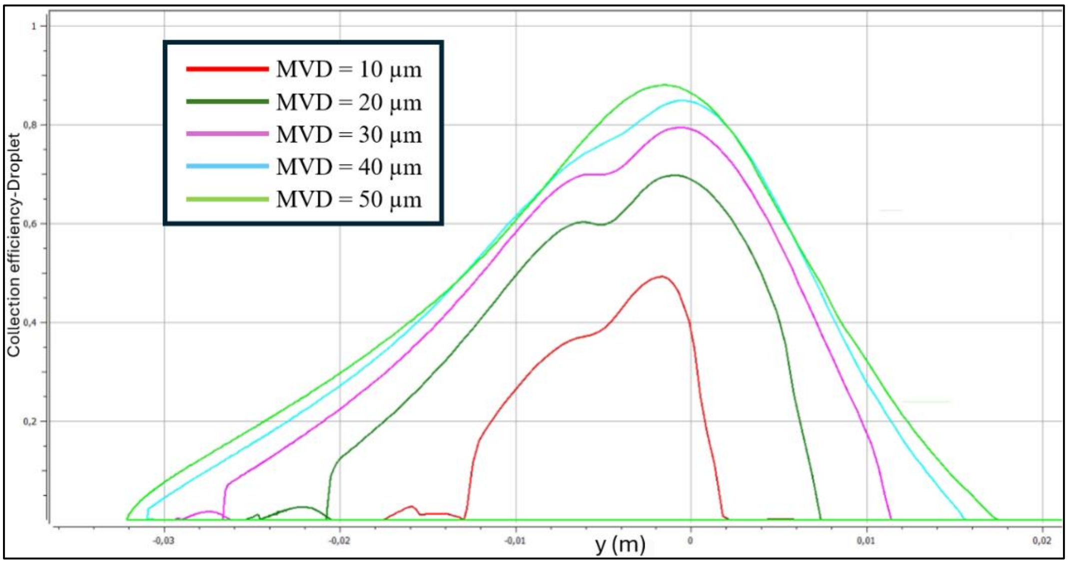

Figure 5.15: The effect of MVD on collection efficiency

5.3.3 Effect of MVD on Performance Degradation

The impact of different MVD values on lift and drag characteristics is examined in Figures 5.16 and 5.17 to evaluate their influence on aerodynamic performance. The results indicate that as the MVD increases, the lift coefficient tends to decrease, while the drag coefficient increases. Although the maximum ice thickness is observed at an MVD of 20 µm, the most significant aerodynamic performance degradation occurs at 50 µm. This is due to the ice being distributed over a much larger area of the airfoil surface. At an MVD of 50 µm, the lift coefficient decreases by up to 17%, while the drag coefficient increases by approximately 325%.

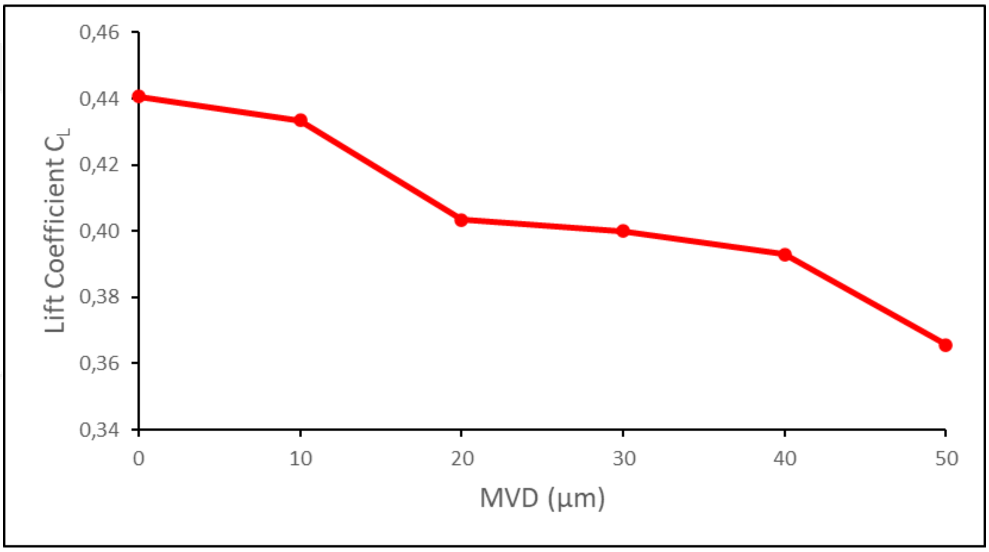

Figure 5.16: The effect of MVD on lift coefficient

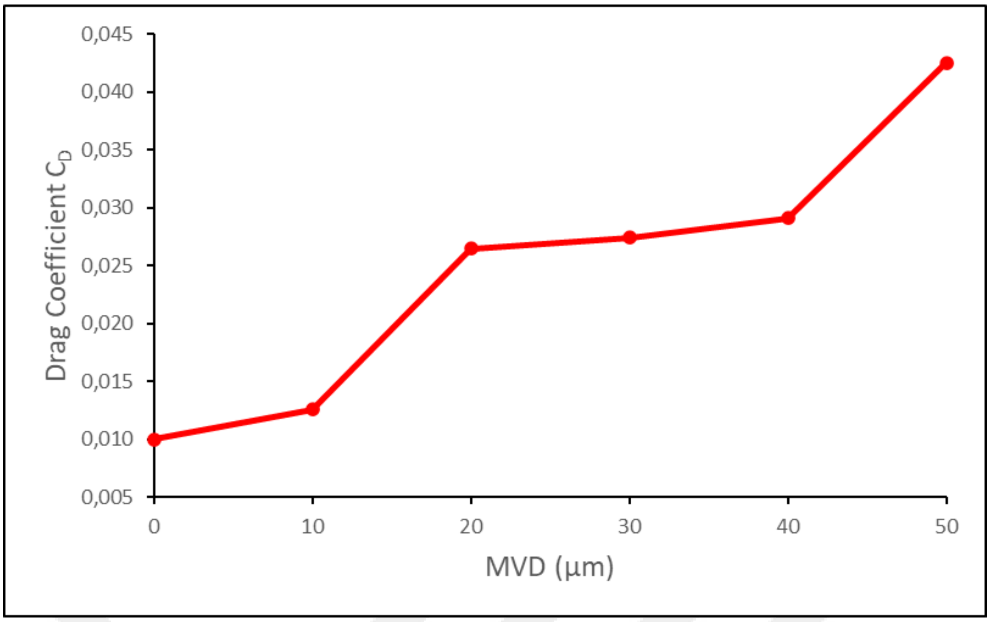

Figure 5.17: The effect of MVD on drag coefficient

5.3.4 Contour Investigation of Turbulent Viscosity at different MVD

Figure 5.18 presents the turbulent viscosity distributions for different MVD values. At a low MVD value of 10 µm, a thin viscous layer forms near the leading edge; however, flow separation tendency remains weak. When the MVD increases to 20 µm, the ice-covered area grows and surface roughness increases. Consequently, the turbulent viscosity region thickens, indicating greater momentum transfer and resulting in a broader impingement area. In particular, at 50 µm, a distinct turbulent zone develops, and boundary layer separation occurs much earlier along the airfoil surface.

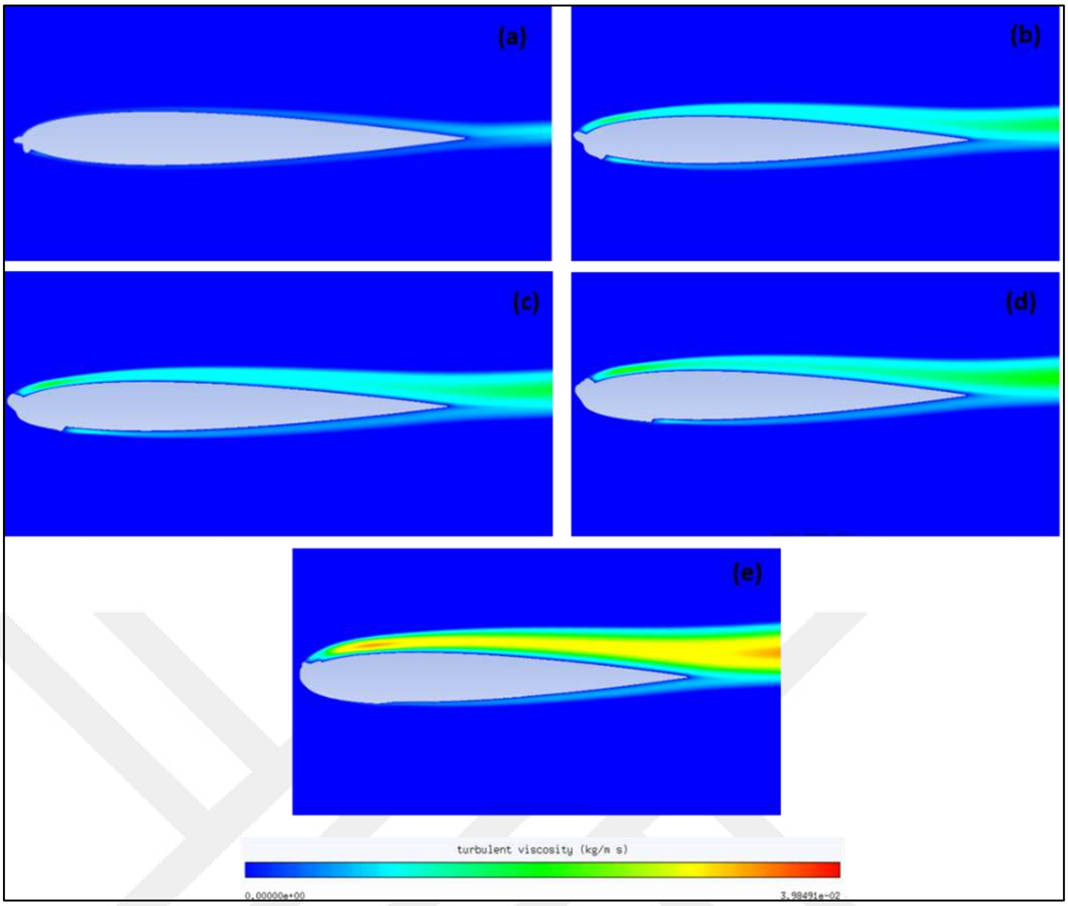

Figure 5.18: Turbulent viscosity contours for MVD (a) 10 (b) 20 (c) 30 (d) 40 (e) 50 µm

5.4 EFFECT OF AIRSPEED ON ICING

The effect of airspeed on ice accretion was investigated using velocities of 50 m/s, 67.056 m/s, 80, m/s, 90 m/s and 100 m/s. The detailed parameters are summarized in the table below.

Table 5.4: Icing conditions for different airspeeds

Simulation Cases	SC17	SC18	SC19	SC20	SC21
AoA [°]	4	4	4	4	4
Temperature [° C]	-5.5	-5.5	-5.5	-5.5	-5.5
Velocity [m/s]	**50**	**67.056**	**80**	**90**	**100**
LWC [g/m^3]	1	1	1	1	1
MVD [µm]	20	20	20	20	20
Exposure Time [s]	360	360	360	360	360

5.4.1 Effect of Airspeed on Ice Shape and Ice Thickness

Figure 5.19 presents the ice shapes obtained at different air speeds. Regardless of the velocity, a double-horn structure is observed in all cases, with one horn forming on the pressure side and the other on the suction side of the airfoil. At lower velocities, the horn geometry tends to be closer to a symmetric configuration, whereas with increasing airspeed it becomes progressively more asymmetric. With increasing velocity, the horns become more pronounced; however, the relative variation in horn geometry is greater at lower speeds. At higher speeds, this variation diminishes, and the influence of horn geometry on the overall ice shape becomes less dominant.

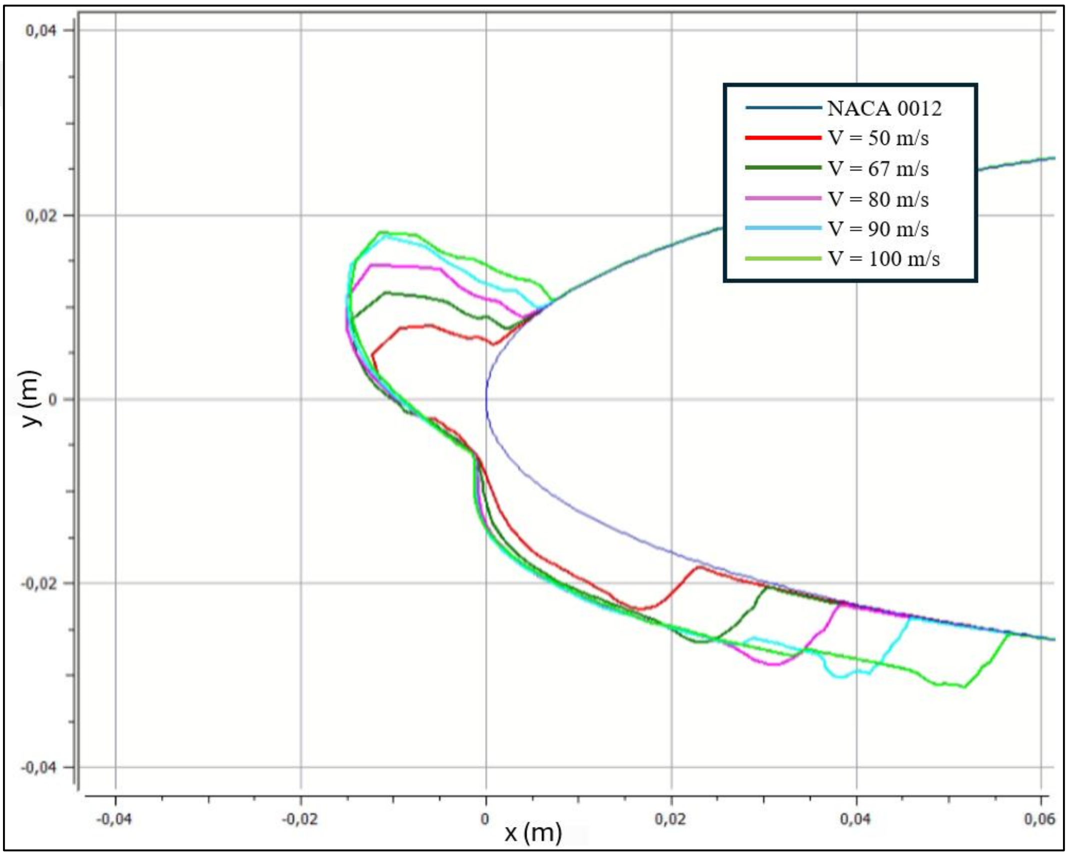

Figure 5.19: The effect of airspeed on ice shape

Figure 5.20 illustrates the variation of ice thickness at different airspeeds. As the horn height increases, particularly on the upper surface, the sharpness of the horn becomes more pronounced, and the longitudinal extent of icing on this surface increases significantly. Analysis of the maximum thickness reveals that it increased by approximately 23% when the velocity rose from 50 m/s to 67 m/s, by around 10% from 67 m/s to 80 m/s, and by about 7% from 80 m/s to 90 m/s. No increase in maximum ice thickness was observed between 90 m/s and 100 m/s. This indicates that beyond 90 m/s, the influence of velocity on maximum thickness becomes minimal, a trend that is also reflected in the aerodynamic performance variations.

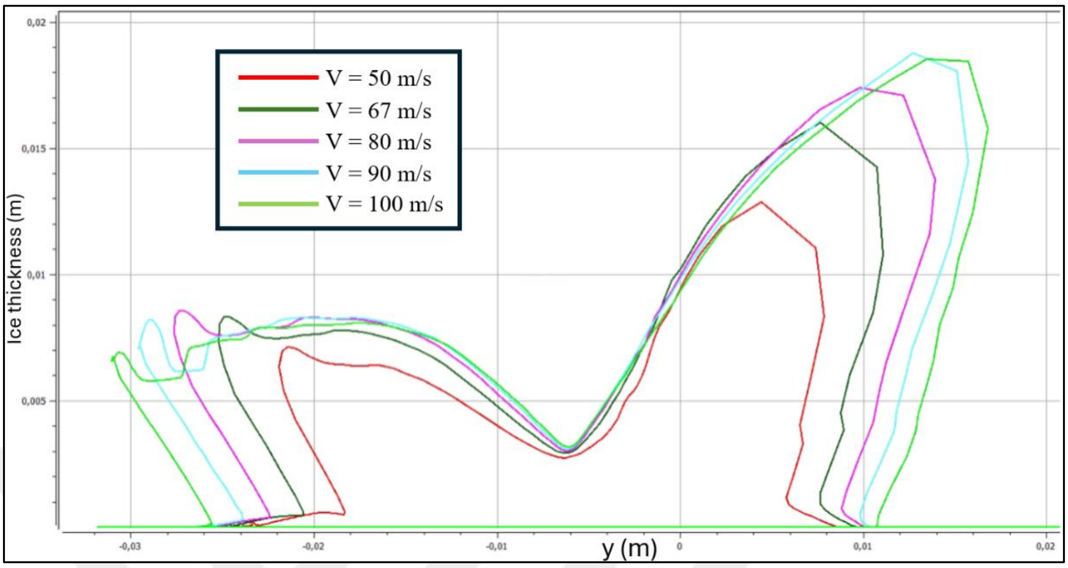

Figure 5.20: The effect of airspeed on ice thickness

5.4.2 Effect of Airspeed on Performance Degradation

Figure 5.21 and Figure 5.22 clearly demonstrate the effects of increasing airspeed on the aerodynamic performance of the airfoil. Increasing airspeed results in a reduction in the lift coefficient and a substantial rise in the drag coefficient. Examination of lift and drag variations also shows that at speeds where significant horn-geometry changes occur (up to 90 m/s), the reduction in lift and increase in drag are more pronounced. Conversely, when horn-geometry changes become less significant, the aerodynamic performance variations are also minimized. At the highest simulated airspeed of 100 m/s, the lift coefficient drops by approximately 15% compared to the clean profile, whereas the drag coefficient increases dramatically by about 315%.

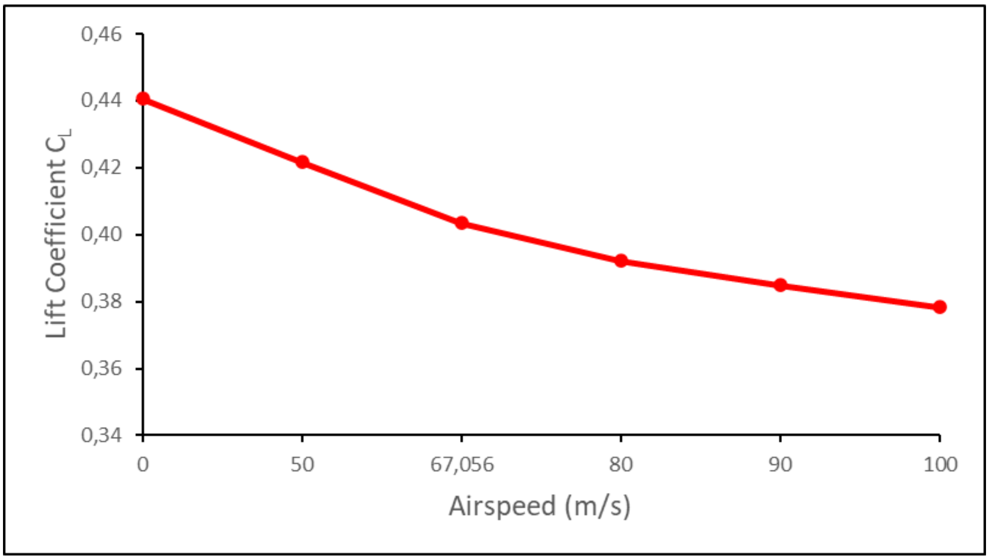

Figure 5.21: The effect of airspeed on lift coefficient

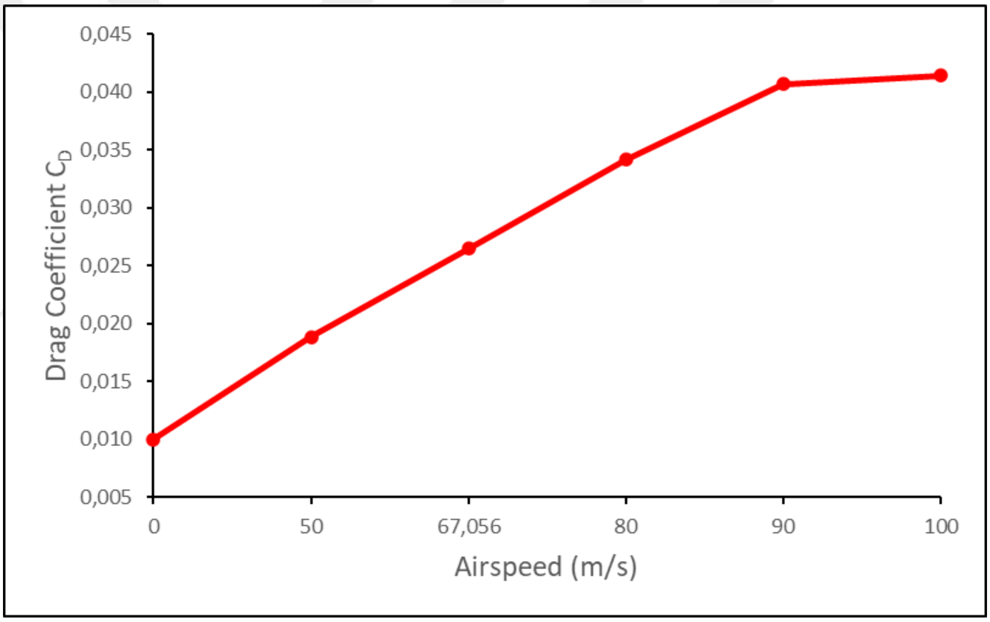

Figure 5.22: The effect of airspeed on drag coefficient

5.5 EFFECT OF EXPOSURE TIME ON ICING

This section focuses on the effect of exposure time on ice accumulation. Time periods of 1, 2, 4, 6 and 8 minutes were used to observe changes in ice growth over time. The detailed icing conditions are listed in the table below.

Table 5.5: Icing conditions for different exposure times

Simulation Cases	SC22	SC23	SC24	SC25	SC26
AoA [°]	4	4	4	4	4
Temperature [° C]	-5.5	-5.5	-5.5	-5.5	-5.5
Velocity [m/s]	67.056	67.056	67.056	67.056	67.056
LWC [g/m^3]	1	1	1	1	1
MVD [µm]	20	20	20	20	20
Exposure Time [s]	**60**	**120**	**240**	**360**	**480**

5.5.1 Effect of Exposure Time on Ice Shape and Ice Thickness

Figure 5.23 illustrates the effect of different exposure times on ice shape formation over the airfoil surface. When the overall structure is examined, the ice formation can be described as a layered growth extending outward from the surface. At an exposure time of 1 minute, the ice accumulation is relatively thin and closely follows the airfoil contour, with minimal protrusion. After an exposure time of 2 minutes, horn-shaped ice formations began to develop more clearly, indicating a transition to more complex ice shapes. At an exposure time of 8 minutes, the ice-covered area reached its maximum extent.

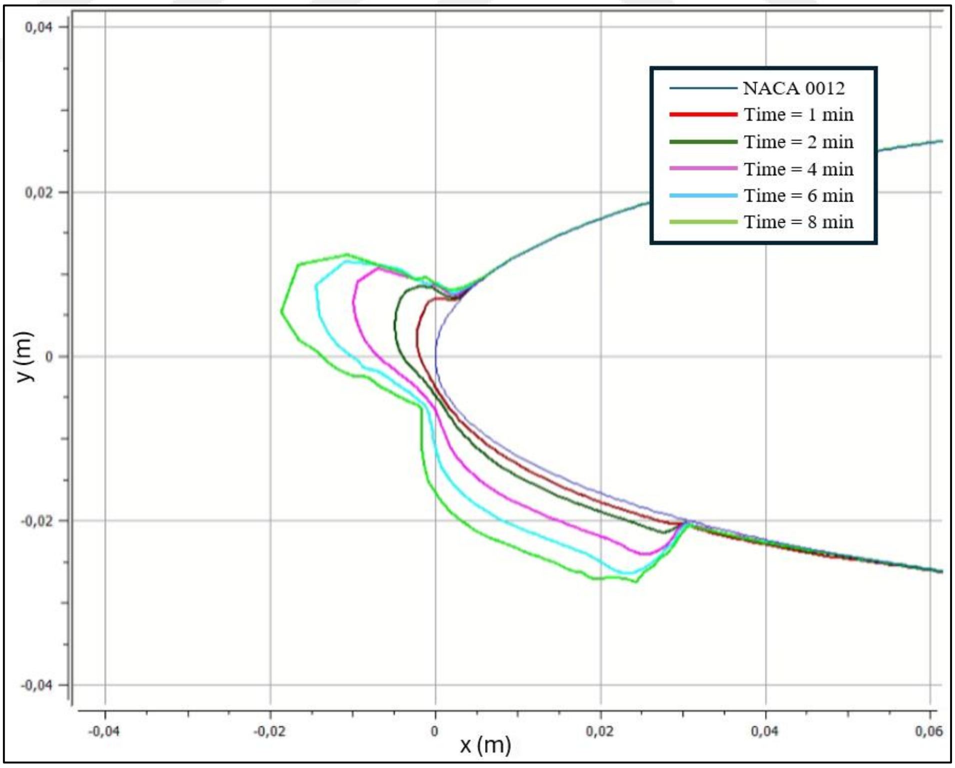

Figure 5.23: The effect of exposure time on ice shape

Figure 5.24 illustrates how ice thickness varies with different exposure times. Ice thickness gradually increases on both the upper and lower surfaces of the airfoil as the exposure time increases. At an exposure time of 1 minute, the maximum ice thickness reaches approximately 0.003 m. By the end of 8 minutes, this value increases significantly, reaching up to 0.02 m.

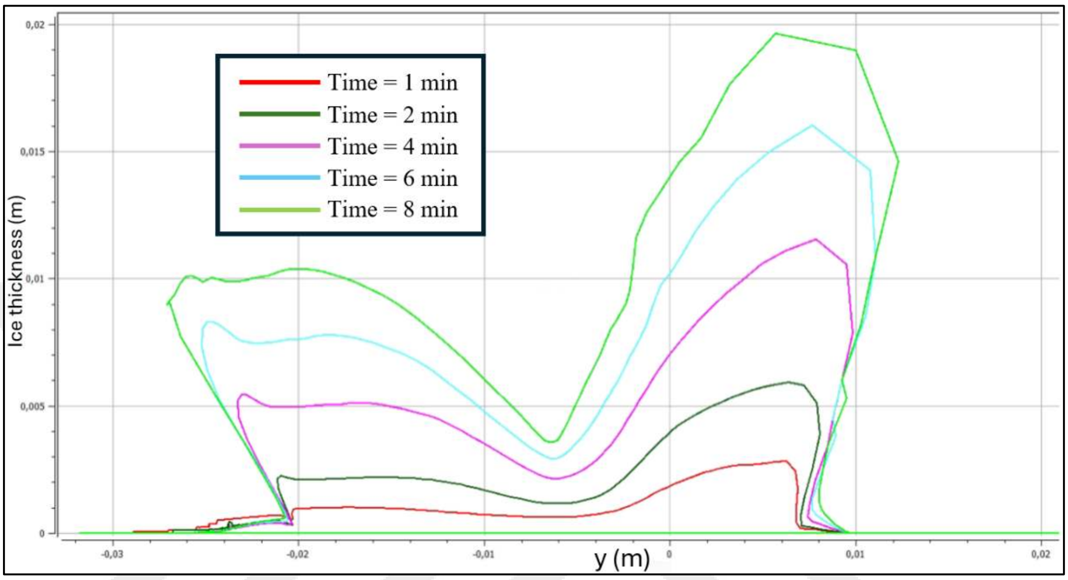

Figure 5.24: The effect of exposure time on ice thickness

5.5.2 Effect of Exposure Time on Performance Degradation

Figure 5.25 and Figure 5.26 present the changes in lift and drag coefficients observed at different exposure times to assess their impact on aerodynamic performance. As expected, the lift coefficient decreased while the drag coefficient increased with increasing exposure time. At an exposure time of 8 minutes, the lift coefficient was observed to decrease by up to 11%, whereas the drag coefficient increased by approximately 175%.

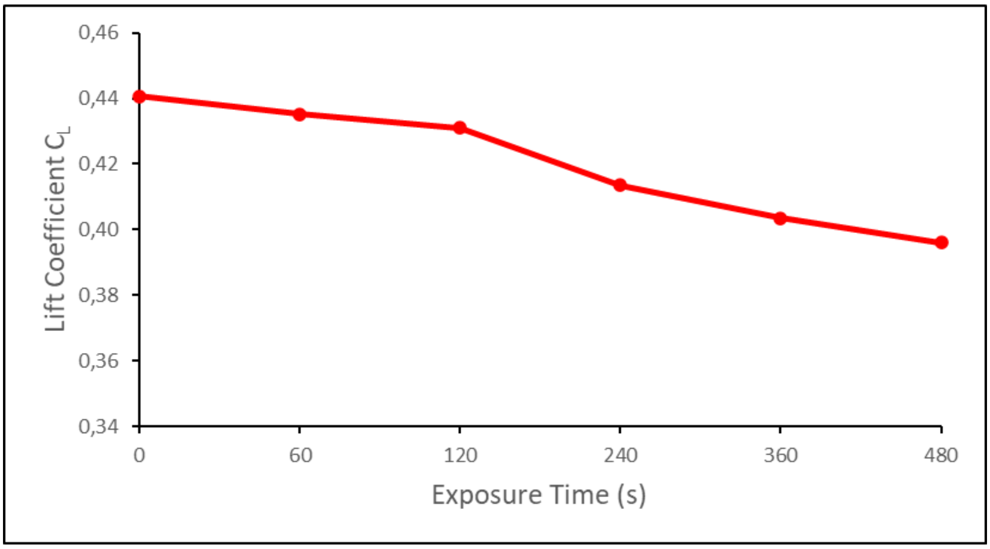

Figure 5.25: The effect of exposure time on lift coefficient

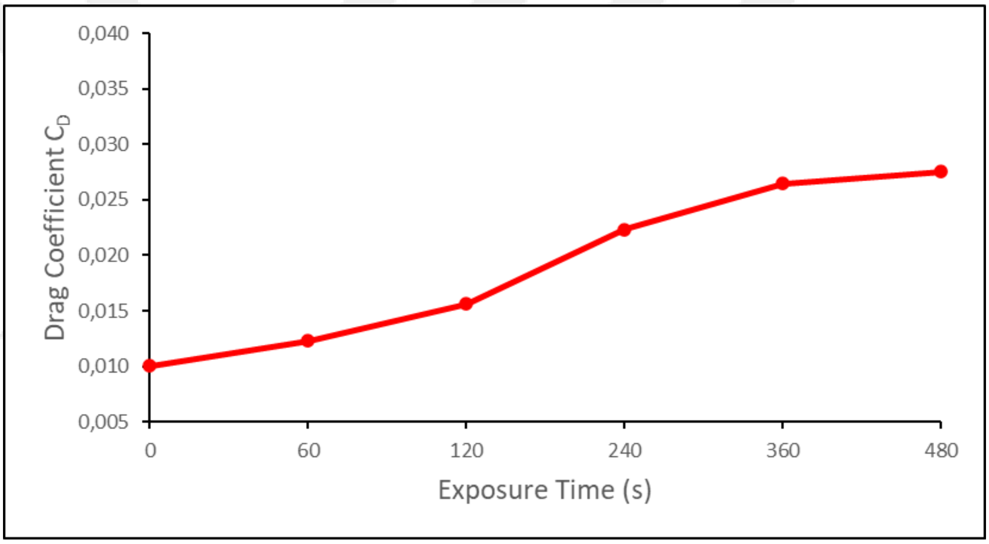

Figure 5.26: The effect of exposure time on drag coefficient

CHAPTER VI
CONCLUSION

In this thesis, various parameters affecting ice formation on the NACA 0012 airfoil have been investigated. In particular, the effects of angle of attack (AoA), liquid water content (LWC), mean volumetric diameter (MVD), airspeed, and exposure time on ice accretion were evaluated. Based on these parameters, the findings obtained are summarized below:

- The results indicate that increasing the angle of attack significantly alters the ice accretion characteristics, leading to asymmetric ice horn development and earlier stall. Aerodynamic evaluations demonstrated a notable decrease in lift up to 56% and a dramatic increase in drag up to 625% due to icing observed specifically at 12° AoA.
- As the liquid water content (LWC) increases, the ice shape becomes more irregular. More ice accumulates on both the upper and lower surfaces of the airfoil, and the maximum ice thickness also increases significantly. This leads to a decrease in lift by up to 12% and an increase in drag by about 260% at the highest LWC of 1.75 g/m^3.
- As the mean volumetric diameter (MVD) increases, ice forms over a larger area on both the upper and lower surfaces of the airfoil, and the ice shape becomes more irregular. At low MVD values, ice is mostly limited near the leading edge and more symmetric. With higher MVD values, ice spreads more widely, especially along the lower surface, reaching up to 0.15 m. Although the maximum ice thickness occurs at an MVD of 20 μm, the most significant decrease in aerodynamic performance happens at 50 μm due to the larger ice-covered area. This causes a decrease in lift by up to 17% and an increase in drag by about 325%.
- As airspeed increases, the ice on the airfoil forms a double-horn shape that becomes more asymmetric at higher speeds. At lower speeds, the horns are more symmetric but show greater variation. Increasing airspeed leads to a decrease in lift and increase in drag. At the highest speed of 100 m/s, lift decreases by about

15% and drag increases by approximately 315%.

- As exposure time increases, ice grows thicker and covers more of the airfoil surface. At 1 minute, ice is thin and follows the airfoil shape closely, but by 8 minutes, ice thickness reaches about 0.02 m and covers the largest area. At an exposure time of 8 minutes, this causes lift to decrease by up to 11% and drag to increase by approximately 175%.

REFERENCES

[1] SPICUGLIA Fabrizio (2024), *Ice Formation on Aircraft* [Photograph], https://panamedia.org/ice-formation-on-aircraft/?lang=en, DoA. 20.08.2025.

[2] POTAPCZUK Mark G. and BERKOWITZ Brian M. (1989*), Experimental investigation of multielement airfoil ice accretion and resulting performance degradation*, NASA Report Number: NASA-TM-101441, https://ntrs.nasa.gov/citations/19890005713, DoA. 20.08.2025.

[3] Bruce Landsberg (2008), "Aircraft Icing", *Safety* Advisor, Weather No 1, pp.1-16, https://www.aopa.org/-/media/files/AOPA/Home/Pilot-Resources/ASI/Safety-Advisors/sa11.pdf, DoA. 20.08.2025.

[4] National Transportation Safety Board (1994), *AIRCRAFT ACCIDENT REPORT*, Report No. NTSB/AAR-96/01, Washington DC.

[5] BRAGG Michael B., BROEREN A.P. and BLUMENTHAL L.A. (2005), "Iced-Airfoil Aerodynamics", *Progress in Aerospace Sciences*, Vol. 41, No. 5, pp. 323-362.

[6] Bureau of Aircraft Accidents Archives (1994), *Crash of an ATR72-212 in Roselawn: 68 killed* [Photograph], https://www.baaa-acro.com/crash/crash-atr72-212-roselawn-68-killed, DoA. 20.08.2025.

[7] CZERNKOVICH Nick (2004), "Understanding In-Flight Icing", *Transport Canada Aviation Safety Seminar*, Vol. 55, No. 1, pp. 1-21.

[8] POLITOVICH M.K., and BELO-PEREIRA Margarida (2019), *Aircraft Icing* [Photograph], Reference Module in Earth Systems and Environmental Sciences, Elsevier.

[9] Advisory Group For Aerospace Research & Development (1997), *Ice Accretion Simulation*, AGARD ADVISORY REPORT 344, https://publications.sto.nato.int/publications/AGARD/AGARD-AR-344/AGARDAR344.pdf, DoA. 08.08.2025.

[10] HEINRICH A., ROSS R., ZUMWALT G., PROVORSE J. and PADMANABHAN V. (1991), *Aircraft Icing Handbook Volume 2 of 3*, FAA Technical Center, Report No. DOT/FAA/CT-88/8-2.

[11] HARDY J.K. (1946), *Protection of aircraft against ice*, British R.A.E, Report No. 3380.

[12] LANGMUIR I. and BLODGETT K.B. (1946), *A mathematical investigation of water droplet trajectories*, Army Air Forces, Report No. 5418.

[13] MESSINGER B.L (1953), "Equilibrium temperature of an unheated icing surface as a function of air speed", *Journal of the aeronautical sciences,* Vol. 20, No. 1, pp. 29-42.

[14] GENT R.W., DART N.P. and CANSDALE J.T. (2000), "Aircraft Icing", *Philosophical Transactions of the Royal Society of London, Series A: Mathematical, Physical and Engineering Sciences*, Vol. 358, No. 1776, pp. 2873-2911.

[15] OLSEN William, SHAW Robert and NEWTON James. (1984), "Ice Shapes and the Resulting Drag Increase for a NACA 0012 Airfoil", *22nd Aerospace Sciences Meeting*, p. 109, Reno, NV, U.S.A.

[16] SHIN Jaiwon and BOND Thomas H. (1992), "Results of an Icing Test on a NACA 0012 Airfoil in the NASA Lewis Icing Research Tunnel", *30th Aerospace Sciences Meeting and Exhibit*, p. 647, Reno, NV, U.S.A.

[17] WRIGHT William B., GENT R.W. and GUFFOND Didier. (1997), *DRA/NASA/ONERA Collaboration on Icing Research: Prediction of Airfoil Ice Accretion – Part 2*, Report No. NAS 1.26: 202349, NASA Technical Reports Server.

[18] LEE Sam and BRAGG Michael B. (1999), "Experimental Investigation of Simulated Large-Droplet Ice Shapes on Airfoil Aerodynamics", *Journal of Aircraft*, Vol. 36, No. 5, pp. 844-850.

[19] KIM Han S. and BRAGG Michael B. (1999), "Effects of Leading-Edge Ice Accretion Geometry on Airfoil Performance", *17th Applied Aerodynamics Conference*, p. 3150, Norfolk, VA, U.S.A.

[20] BROEREN A.P., BRAGG Michael B. and ADDY Harold E. (2004), "Effect of Intercycle Ice Accretions on Airfoil Performance", *Journal of Aircraft*, Vol. 41, No. 1, pp. 165-174.

[21] CHI X., LI Y., ADDY H.E., CHOO Y.K., SHIH T and CHEN H. (2005), "A Comparative Study Using CFD to Predict Iced Airfoil Aerodynamics", *43rd AIAA Aerospace Sciences Meeting and Exhibit*, p. 1371, Reno, Nevada.

[22] SON Chankyu, OH Sejong and YEE Kwanjung (2012), "Quantitative Analysis of a Two-Dimensional Ice Accretion on Airfoils", *Journal of Mechanical Science and Technology*, Vol. 26, No. 4, pp. 1059-1071.

[23] POURYOUSSEFI Sohrab Gholamhosein, MIRZAEI Masoud, NAZEMI Mohammad-Mahdi, FOULADI Mojtaba and DOOSTMAHMOUDI Alireza (2016), "Experimental Study of Ice Accretion Effects on Aerodynamic Performance of an NACA 23012 Airfoil", *Chinese Journal of Aeronautics*, Vol. 29, No. 3, pp. 585-595.

[24] SZNAJDER Janusz, SIERADZKI Adam, STALEWSKI Wieńczysław (2017), "Determination of Ice Deposit Shape and Ice Accretion Rate on Airfoil in Atmospheric Icing Conditions and Its Effects on Airfoil Characteristics", *Journal of KONES*, Vol. 24, No. 2, pp. 271-278.

[25] LU Hao, XU Yongzhong, LI Hongchang and ZHAO Wenjun (2023), "Numerical Study on Glaze Ice Accretion Characteristics Over Time for a NACA 0012 Airfoil", *Coatings*, Vol. 14, No. 1, p. 55.

[26] BHATIA Dinesh, WAHAIBI Al Yaqadan Shaaban al (2020), "A Numerical Investigation into the Impact of Icing on the Aerodynamic Performance of Aerofoils", *IOP Conference Series: Materials Science and Engineering*, Vol. 831, No. 1, p. 012007.

[27] YIRTICI Ozcan, TUNCER Ismail H. and OZGEN Serkan (2016), "Ice Accretion Prediction on Wind Turbines and Consequent Power Losses", *Journal of Physics: Conference Series*, Vol. 753, No. 2, p. 022022.

[28] KRØGENES Julie, BRANDRUD Lovisa, HANN Richard, BARTL Jan, BRACCHI Tania and SÆTRAN Lars (2017), "Aerodynamic Performance of the NREL S826 Airfoil in Icing Conditions", *Wind Energy Science Discussions*, pp. 1-17, DOI: 10.5194/wes-2017-39.

[29] HANN Richard, HEARST R. Jason, SÆTRAN Lars Roar and BRACCHI Tania (2020), "Experimental and Numerical Icing Penalties of an S826 Airfoil at Low Reynolds Numbers", *Aerospace*, Vol. 7, No. 4, p. 46.

[30] HANN Richard and JOHANSEN Tor Ame (2021), "UAV Icing: The Influence of Airspeed and Chord Length on Performance Degradation", *Aircraft Engineering and Aerospace Technology*, Vol. 93, No. 5, pp. 832-841.

[31] FAJT Nicolas, HANN Richard and LUTZ Thorsten (2019), "The Influence of Meteorological Conditions on the Icing Performance Penalties on a UAV Airfoil", *8th European Conference for Aeronautics and Space Sciences (EUCASS)*, Madrid, Spain.

[32] CAO Y., MA C., ZHANG Q. and SHERIDAN J. (2012), "Numerical simulation of ice accretions on an aircraft wing", *Aerospace Science and Technology,* Vol. 23, No. 1, pp. 296-304.

[33] Ansys Inc. (2025), *FENSAP-ICE User Manual,* Release 2025 R2, USA.

[34] SHIN Jaiwon, BERKOWITZ Brian, CHEN Hsun and CEBECI Tuncer (1991), "Prediction of Ice Shapes and Their Effect on Airfoil Performance", *29th Aerospace Sciences Meeting*, p. 264, Reno, NV, U.S.A.

[35] LADSON Charles L. (1988), *Effects of Independent Variation of Mach and Reynolds Numbers on the Low-Speed Aerodynamic Characteristics of the NACA 0012 Airfoil Section*, Report No. NASA Technical Memorandum 4074, National Aeronautics and Space Administration.

[36] WRIGHT William B. (2002), *User Manual for the NASA Glenn Ice Accretion Code LEWICE*, Version 2.2.2, Report No. NASA CR-2002-211793, National Aeronautics and Space Administration.

[37] LIU T., QU K., CAI J. and PAN S. (2019), "A three-dimensional aircraft ice accretion model based on the numerical solution of the unsteady Stefan problem", *Aerospace Science and Technology*, Vol. 93, Article Number 105328.

[38] HOMOLA M.C., VIRK M.S., WALLENIUS T., NICKLASSON P.J, and SUNDSBØ P.A. (2010), "Effect of atmospheric temperature and droplet size variation on ice accretion of wind turbine blades", *Journal of wind engineering and industrial aerodynamics,* Vol. 98, No. 12, pp. 724-729.